Normalized particle size distribution for remote sensing application

Julien Delanoë, Andrew J. Heymsfield, Alain Protat, Aaron Bansemer, R. J. Hogan

▶ **To cite this version:**

Julien Delanoë, Andrew J. Heymsfield, Alain Protat, Aaron Bansemer, R. J. Hogan. Normalized particle size distribution for remote sensing application. Journal of Geophysical Research: Atmospheres, 2014, 119 (7), pp.4204-4227. 10.1002/2013JD020700 . hal-00979328

HAL Id: hal-00979328
https://hal.science/hal-00979328

Submitted on 23 Apr 2016

HAL is a multi-disciplinary open access archive for the deposit and dissemination of scientific research documents, whether they are published or not. The documents may come from teaching and research institutions in France or abroad, or from public or private research centers.

L'archive ouverte pluridisciplinaire **HAL**, est destinée au dépôt et à la diffusion de documents scientifiques de niveau recherche, publiés ou non, émanant des établissements d'enseignement et de recherche français ou étrangers, des laboratoires publics ou privés.

AGU PUBLICATIONS

JGR

Journal of Geophysical Research: Atmospheres

RESEARCH ARTICLE

10.1002/2013JD020700

Key Points:

- This study describes a normalization technique to represent the PSD
- In situ measurements are covering a large variety of ice clouds
- This new data set also includes direct measurements of IWC

Correspondence to:
J. M. E. Delanoë,
julien.delanoe@latmos.ipsl.fr

Citation:
Delanoë, J. M. E., A. J. Heymsfield, A. Protat, A. Bansemer, and R. J. Hogan (2014), Normalized particle size distribution for remote sensing application, *J. Geophys. Res. Atmos.*, *119*, 4204-4227, doi:10.1002/2013JD020700.

Received 7 AUG 2013
Accepted 13 JAN 2014
Accepted article online 15 JAN 2014
Published online 14 APR 2014

Normalized particle size distribution for remote sensing application

J. M. E. Delanoë[1], A. J. Heymsfield[2], A. Protat[3], A. Bansemer[2], and R. J. Hogan[4]

[1]LATMOS/UVSQ/IPSL/CNRS, Guyancourt, France, [2]NCAR, Boulder, Colorado, USA, [3]Centre for Australian Weather and Climate Research, Melbourne, Victoria, Australia, [4]Department of Meteorology, University of Reading, Reading, UK

Abstract The ice particle size distribution (PSD) is fundamental to the quantitative description of a cloud. It is also crucial in the development of remote sensing retrieval techniques using radar and/or lidar measurements. The PSD allows one to link characteristics of individual particles (area, mass, and scattering properties) to characteristics of an ensemble of particles in a sampling volume (e.g., visible extinction (σ), ice water content (IWC), and radar reflectivity (Z)). The aim of this study is to describe a normalization technique to represent the PSD. We update an earlier study by including recent in situ measurements covering a large variety of ice clouds spanning temperatures ranging between −80°C and 0°C. This new data set also includes direct measurements of IWC. We demonstrate that it is possible to scale the PSD in size space by the volume-weighted diameter D_m and in the concentration space by the intercept parameter N_0^* and obtain the intrinsic shape of the PSD. Therefore, by combining N_0^*, D_m, and a modified gamma function representing the normalized PSD shape, we are able to approximate key cloud variables (such as IWC) as well as cloud properties which can be remotely observed (such as Z) with an absolute mean relative error smaller than 20%. The underlying idea is to be able to retrieve the PSD using two independent measurements. We also propose parameterizations for ice cloud key parameters derived from the normalized PSD. We also investigate the effects of uncertainty present in the ice crystal mass-size relationships on the parameterizations and the normalized PSD approach.

1. Introduction

Remote sensing instruments give us the potential to tackle issues such as the role of clouds in climate and also the cloud processes involved. These instruments, active or passive which can be located on different platforms, require critical assumptions to convert raw measurements into cloud properties. Most retrieval techniques use lookup tables or empirical relationships to link measured parameters to microphysical cloud properties, either through a retrieval process or an instrument simulator. The particle size distribution (PSD) of ice cloud particles can be defined as the concentration of ice particles as a function of their maximum dimension. It allows one to characterize the particles per unit of volume and their bulk properties. For instance, it is straightforward to calculate the ice water content (IWC) from the combination of the mass as the function of the maximum dimension (hereafter $M(D)$, where D is the maximum dimension of the ice crystal as derived by finding the minimum diameter of a circle that fully encloses the two-dimensional image of a particle) of a particle and the PSD. The characterization of the PSD is a challenging task since it greatly depends on meteorological conditions and location.

Some recent combined radar and lidar retrieval techniques use the normalized PSD approach [*Delanoë et al.*, 2007; *Delanoë and Hogan*, 2008, 2010; *Szyrmer et al.*, 2012] to simplify the relationships between cloud properties and instrument measurements such as radar reflectivity or Doppler velocity. This paper aims to update the work of *Delanoë et al.* [2005], by considering direct measurements of the IWC, yielding progresses made with microphysical probes knowledge of $M(D)$.

We also propose a new technique to estimate the optimal intrinsic shape of the PSD by minimizing the differences between moments of the PSD, such as visible extinction and radar reflectivity, calculated from the normalized and the non-normalized approach.

In section 2, we present the normalized PSD concept for ice clouds. A description of the data and the main microphysical assumptions involved in the study is given in section 3. The impact of the normalization on the PSD, the cloud variables (such as IWC, extinction, and such) as well as cloud properties which can

 ©2014. American Geophysical Union. All Rights Reserved.

be remotely observed (such as radar reflectivity or the terminal fall velocity) is described in section 4. We propose a parameterization for the normalized PSD and key cloud variables and its assessment in sections 5 and 6. We will then conclude and discuss the results in the last section.

2. The Normalized Particle Size Distribution Concept

In this section we summarize the normalized PSD concept of *Delanoë et al.* [2005]. In order to adapt the framework introduced by *Testud et al.* [2001] for rain drop spectra to the case of ice particles, *Delanoë et al.* [2005] used the equivalent melted diameter (D_{eq}). Using this framework, D_{eq} can be then be calculated using the following relationship:

$$D_{eq} = \left[\frac{6\,M(D)}{\pi\rho_w}\right]^{\frac{1}{3}} \text{ [m]}, \tag{1}$$

where ρ_w is the density of water (1000 kg/m^3). By definition $D_{eq} \leq D$, the particle, once melted, cannot be larger than its maximum diameter. It would correspond to an ice density exceeding the density of solid ice (917 kg/m^3), which is obviously not possible.

$M(D)$ is commonly represented using a power law relationship and derived using PSD spectra combined with bulk measurements of IWC [*Brown and Francis*, 1995; *Lawson and Baker*, 2006; *Heymsfield et al.*, 2010]. The mass-size relationship used in *Delanoë et al.* [2005] study came from *Brown and Francis* [1995], employing a very limited data set. For instance, the observations reported by *Brown and Francis* [1995] were acquired primarily at temperatures from −20°C to −30°C, with masses dominated by particles in the 200–800 micron size range. Although this relationship can be applied to many kinds of ice clouds [*Heymsfield et al.*, 2010] and it is still used in many radar-lidar retrieval algorithms [*Delanoë and Hogan*, 2008, 2010], it may not be the most appropriate relationships for all ice clouds met in this study. Therefore, we used the dedicated mass-size relationships developed from direct IWC measurement and provided in *Heymsfield et al.* [2010]. These relationships will be described later on in the data description section 3.3.

The particle size distribution $N(D)$ can also be rewritten in terms of D_{eq} as by definition $N_{eq}(D_{eq})\mathrm{d}D_{eq} = N(D)\mathrm{d}D$ for a given diameter bin. Ice water content is therefore proportional to the third moment of $N_{eq}(D_{eq})$:

$$\mathrm{IWC} = \frac{\pi\rho_w}{6}\int_0^\infty N(D_{eq})D_{eq}^3\mathrm{d}D_{eq}, \tag{2}$$

The basis of the normalized approach is to scale both diameter and concentration (extensive variable) parameters, and it was introduced by *Sekhon and Srivastava* [1971] for the drop size distribution. They used the median volume diameter and a number density as scaling parameters. However, a specific shape was assigned to the drop size distribution to link the scaling parameters; the normalization was considered as a single-moment normalization. This constraint was released by *Testud et al.* [2001], who showed that it was not necessary to fix the drop size distribution shape. Later on, *Lee et al.* [2004] demonstrated that it was possible to normalize the PSD using different combinations of moments of the particle size distribution. Therefore, the choice of parameters which scale the concentration and the diameter is crucial. As the water content remains a key variable for clouds, it appeared therefore useful to make the normalized PSD independent from this variable.

Testud et al. [2001] and *Delanoë et al.* [2005] defined the mean volume-weighted diameter as the ratio of the fourth and the third moments of the PSD in terms of D_{eq} (note that the third moment corresponds to LWC or IWC):

$$D_m = \frac{\int_0^\infty N(D_{eq})D_{eq}^4\mathrm{d}D_{eq}}{\int_0^\infty N(D_{eq})D_{eq}^3\mathrm{d}D_{eq}}. \tag{3}$$

Assuming that the number concentration can be scaled by a normalization factor called N_0^*, we can write

$$N(D_{eq}) = N_0^* F(D_{eq}/D_m), \tag{4}$$

©2014. American Geophysical Union. All Rights Reserved.

where the function F in (4) represents a mathematical function and will be described in detail later in the paper. F will be referred to as the "shape" of the distribution in the following. If we replace $N(D_{\mathrm{eq}})$ in (3) by equation (4), we obtain

$$D_m = \frac{\int_0^\infty N_0^* F(D_{\mathrm{eq}}/D_m) D_{\mathrm{eq}}^4 \mathrm{d}D_{\mathrm{eq}}}{\int_0^\infty N_0^* F(D_{\mathrm{eq}}/D_m) D_{\mathrm{eq}}^3 \mathrm{d}D_{\mathrm{eq}}}. \tag{5}$$

Then we define X as

$$X = D_{\mathrm{eq}}/D_m, \tag{6}$$

and we rewrite expression (5) in terms of X

$$D_m = \frac{D_m^5 N_0^* \int_0^\infty F(X) X^4 \mathrm{d}X}{D_m^4 N_0^* \int_0^\infty F(X) X^3 \mathrm{d}X}. \tag{7}$$

After simplifications, (7) leads to

$$\int_0^\infty F(X) X^4 \mathrm{d}X = \int_0^\infty F(X) X^3 \mathrm{d}X = C, \tag{8}$$

where C is a constant. Combining (2), (4), and (8), IWC can be expressed as a function of N_0^* and D_m:

$$\mathrm{IWC} = \frac{\pi \rho_w}{6} N_0^* D_m^4 C. \tag{9}$$

C was arbitrarily chosen by *Testud et al.* [2001] to be equal to $\Gamma(4)/4^4$ and to correspond to the intercept parameter of an exponential distribution.

N_0^* follows therefore an expression of the form

$$N_0^* = \frac{4^4}{\pi \rho_w} \frac{\mathrm{IWC}}{D_m^4} \; [\mathrm{m}^{-4}]. \tag{10}$$

And in terms of moments of the equivalent PSD

$$N_0^* = \frac{4^4}{6} \frac{\left[\int_0^\infty N(D_{\mathrm{eq}}) D_{\mathrm{eq}}^3 \mathrm{d}D_{\mathrm{eq}}\right]^5}{\left[\int_0^\infty N(D_{\mathrm{eq}}) D_{\mathrm{eq}}^4 \mathrm{d}D_{\mathrm{eq}}\right]^4} \; [\mathrm{m}^{-4}]. \tag{11}$$

The function F in (4) is the "unified" size distribution shape given by *Delanoë et al.* [2005] and has been found to fit measured size distributions when they are appropriately normalized and can be described as

$$F(\alpha, \beta, X) = \beta \frac{\Gamma(4)}{4^4} \frac{\Gamma\left(\frac{\alpha+5}{\beta}\right)^{4+\alpha}}{\Gamma\left(\frac{\alpha+4}{\beta}\right)^{5+\alpha}} X^\alpha \exp\left[-\left(X \frac{\Gamma\left(\frac{\alpha+5}{\beta}\right)}{\Gamma\left(\frac{\alpha+4}{\beta}\right)}\right)^\beta\right], \tag{12}$$

where α and β allow one to adjust the shape to the measured normalized PSD. *Delanoë et al.* [2005] estimated the α and β coefficients for the modified gamma shape using in situ data base. Unfortunately, the data set used in that study did not include direct IWC measurements, which made it impossible to find an optimal $M(D)$. In addition to that, this data set did not adjust the PSD to account for shattering of small particles.

©2014. American Geophysical Union. All Rights Reserved.

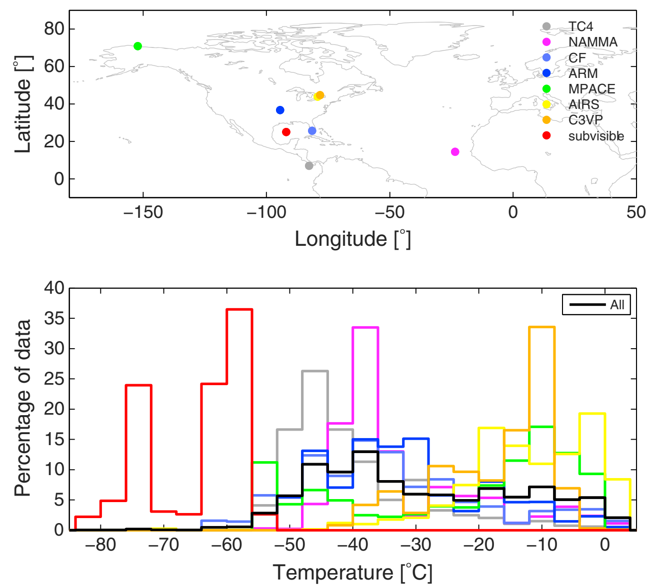

Figure 1. Probability distribution of the data as a function of temperature, for (top) each field campaign (TC4, NAMMA,CRYSTAL-FACE, ARM, C3VP, AIRS, and Subvisible) and (bottom) the whole data set.

3. Data Description

3.1. Presentation of the Data

In this study we used midlatitude, high-latitude, and low-latitude data sets. The data are described in detail in *Heymsfield et al.* [2013]. Midlatitude data are from the Atmospheric Radiation Measurement (ARM) 2000 campaign, an intensive observing period including three cold cirrus cloud flights in synoptically generated ice clouds over Oklahoma. Convectively generated tropical cirrus and anvil data from Florida are from citation aircraft from CRYSTAL-FACE (Cirrus Regional Study of Tropical Anvils and Cirrus-Layers-Florida Area Cirrus Experiment). These data were collected in 2002 and also include very cold temperature cirrus sampled by the WB57F aircraft during CRYSTAL-FACE and will be referred to as Subvisible in the text. Subvisible also includes data from one WB57F aircraft flight between Houston and Costa Rica during the Pre-Aura Validation Experiment; more details can be found in *Schmitt and Heymsfield* [2009].

More recent tropical data are also included in this study. NAMMA (NASA African Monsoon Multidisciplinary Analyses, http://airbornescience.nsstc.nasa.gov/namma/) campaign, which took place in Western Africa in 2006, provided a dozen convectively generated ice and mixed-phase clouds. Some convectively generated ice clouds sampled near Costa Rica in 2008 from the TC4 (Tropical Clouds, Convection, Chemistry, and Climate) [*Toon et al.*, 2010] campaign are also included in the study. Synoptically generated ice cloud layers with embedded convection and supercooled liquid water are from the Alliance Icing Research Study II (AIRS-2); there were seven flights over the Toronto area [see *Isaac et al.*, 2005]. The study also includes three flight data collected in 2006–2007 during the CloudSat/CALIPSO validation Project (C3VP) in the area of Montreal, Canada. Arctic data are from the Mixed-Phase Arctic Cloud Experiment (M-PACE) [*Verlinde et al.*, 2007], 13 flights in Prudhoe Bay, Alaska, area. The locations where the campaigns took place are presented in Figure 1 (top). Note that air temperatures for all field programs were measured with a Rosemount temperature probe. The distribution of the data as a function of temperature is depicted in Figure 1 (bottom). The black line, which represents the full data set, shows that most of the data spans between −50°C and 0°C with a few data collected at very cold temperatures. TC4 and NAMMA data show a monomodal distribution with peaks at −45°C and about −40°C, respectively. On the other hand, CRYSTAL-FACE and ARM have a flatter distribution with no obvious peaks. The M-PACE measurements correspond to both very cold clouds (colder than −40°C) and clouds between −20°C and 0°C where we occasionally detected the presence of supercooled water (discussed later). The C3VP and AIRS data were collected in warm ice clouds with a peak centered at −10°C for C3VP and ice clouds not colder than −40°C. The coldest ice particles are from “Subvisible” with temperatures spanning from −80°C to −60°C.

©2014. American Geophysical Union. All Rights Reserved.

Table 1. Number of 5 s PSD Used in the Study for Each Campaign and Its Percentage of Whole Data

Campaign	Number of 5 s PSD Used in the Study	Percentage of Whole Data
TC4	13,779	25
NAMMA	9,315	16.8
CRYSTAL-FACE	11,966	21.7
ARM	6,187	11.2
M-PACE	2,368	4.3
C3VP	3,348	6
AIRS	7,867	14.2
Subvisible	455	0.8

PSDs were acquired using the following probes, including: 2-D-Cloud and Precipitation (2DC-2DP) probes, Droplet Measurement Technologies Precipitation Imaging Probes (PIP), and High Volume Precipitation Spectrometer (HVPS). The number of 5 s PSD used in the study is recalled for each campaign in Table 1. Probe combinations and diameter ranges for each field campaign are given in Table 2. For the Subvisible data set, data were also collected from a video ice particle sampler [*Schmitt and Heymsfield*, 2009]. A two-dimensional stereo (2D-S) probe was also used for the TC4 analysis (10 μm to > 1 mm). Total condensed water contents (TWC), ice plus liquid when present, were measured with a Counterflow Virtual Impactor or a Cloud Spectrometer and Impactor (CVI and CSI, respectively) for TWC > 0.01 g m^{-3}.

Direct measurements of ice water content above a lower cutoff particle diameter of about 6 μm were obtained from the Counterflow Virtual Impactor (CVI) [*Twohy et al.*, 1997] and a related Cloud Spectrometer and Impactor (CSI) probe. The overall uncertainty of the CVI is about 13% at water contents of 0.05 to 1.0 g m^{-3}. Uncertainty increases to 16% for the minimum detectable IWC of about 0.01 g m^{-3}. The probe is saturated at IWCs above about 2 g m^{-3} [*Twohy et al.*, 1997]. IWC for the Subvisual data set was measured by the University of Colorado closed-path tunable diode laser hygrometer (CLH) for CRYSTAL-FACE.

3.2. Data Processing and Quality Control

In situ data required extensive processing and quality control. For instance, the 2-D probe PSD data are processed to account for ice shattering using particle interarrival times [see *Field et al.*, 2006]. Because of the ice shattering issue, the Forward Scattering Spectrometer Probe or Cloud and Aerosol Spectrometer probes data are not used for small particles. *Heymsfield et al.* [2013] justified this approach by comparing the PSDs with and without the small-particle data to observations from the 2D-S probe from TC4. The impact of the shattering effect is investigated in section A1. Liquid water could artificially increase extinction and influence the ice PSD. In the data set, liquid water was detected and its content estimated from a Rosemount Icing Probe. Liquid water encounters were infrequent and have been filtered out of the data set. The minimum diameters used in this study are 50 μm (TC4/NAMMA/M-PACE/ARM/CRYSTAL-FACE/C3VP/AIRS). The impact of not using particles below 50 μm is discussed in section A2 using 2D-S TC4 data. The Subvisible data are the only data set using ice particle data below 50 μm. This is warranted for two reasons. First, the measurements are made with a probe with a relatively large sample volume for small particles and directly captures the particles and images them rather than with other instruments. The second reason is that at the

Table 2. Probes Used in Each Campaign and Diameter Ranges Available

Campaign	Probes Used	Diameter Range	Condensed Water Content
TC4	2D-S + CIP + PIP	20 μm to > 1 mm	CVI
NAMMA	CIP + PIP	50 μm to > 6 mm	CVI
CRYSTAL-FACE	2DC + HVPS	50 μm to > 1 cm	CVI
ARM	2DC + 2DP	25 μm to > 1 cm	CVI
M-PACE	2DC + 2DP	50 μm to > 1 cm	CSI
C3VP	2DC + 2DP	50 μm to > 1 cm	CSI
AIRS	2DC + 2DP	50 μm to > 1 cm	CVI
Subvis	2DC + VIPS	10 μm to > 800 μm	CLH/Harvard

©2014. American Geophysical Union. All Rights Reserved.

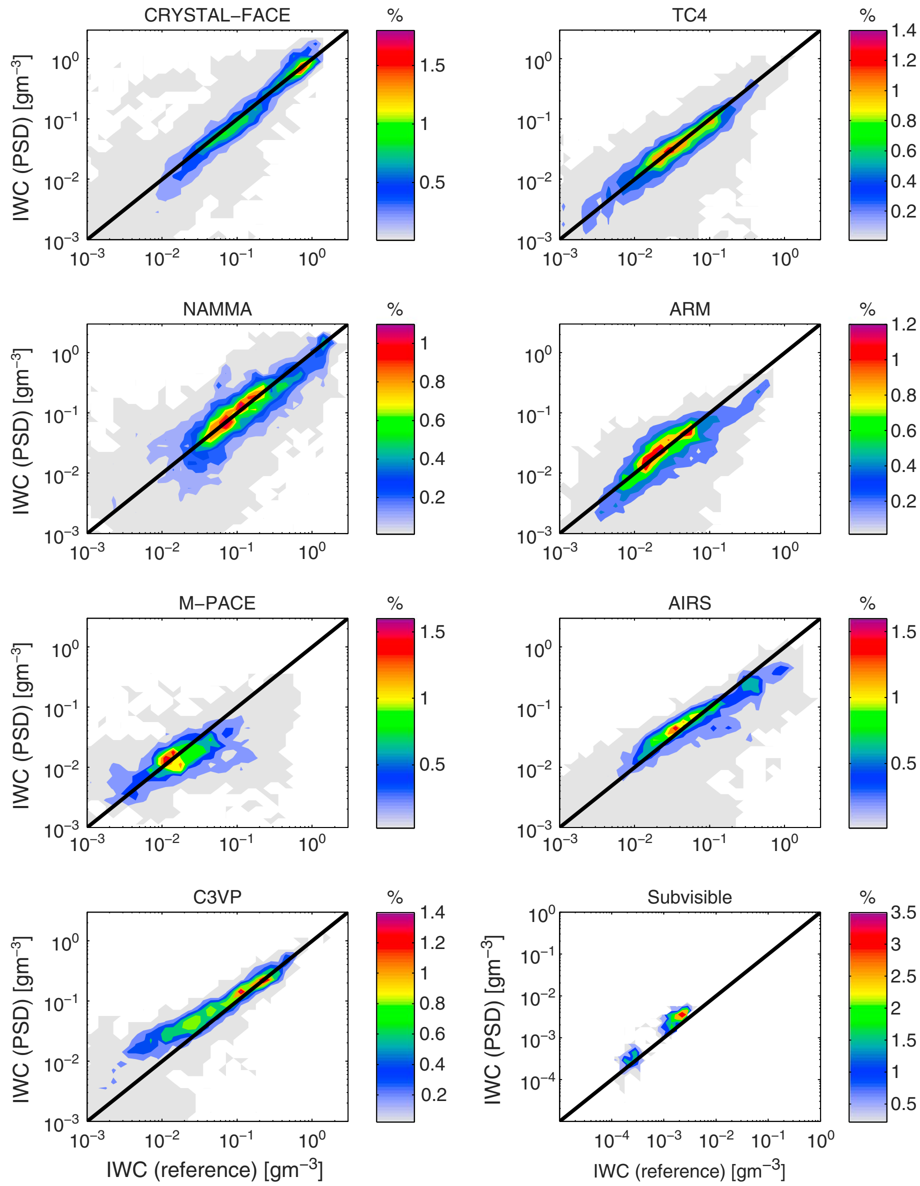

Figure 2. Probability distribution plots of IWC calculated from the PSD as a function of the reference IWC derived from CSI, CVI, or equivalent, for each field campaign (CRYSTAL-FACE, TC4, NAMMA, ARM, M-PACE, C3VP, AIRS, and Subvisible).

very low temperatures associated with the Subvisible data, it is likely that the small particles are numerous compared to warmer temperatures.

3.3. Mass and Area Relationship Assumptions for the Calculation of Cloud and Observed Variables

As noted earlier, the mass-size relationship assumption is crucial when we apply the normalized PSD approach as we need to compute the equivalent melted diameter. Fortunately, in situ data involved here contain CVI, CSI, or equivalent measurements which allow one to measure IWC with only a few assumptions and this IWC will serve as a reference, hereafter IWC_{ref}. Note again that no bulk measurement was available in the *Delanoë et al.* [2005] study.

In our study we used different $M(D)$ described in *Heymsfield et al.* [2010] which are based on direct measurements of the IWC. These $M(D)$ have been combined with the particle size distribution to derive several IWC estimates. We selected the $M(D)$ which gave us a better match to IWC_{ref} for each campaign. The best $M(D)$ will be referred to as the "retrieved" $M(D)$ in our study. As mentioned in *Heymsfield et al.* [2010], each mass-size relationship was derived for specific cloud conditions, for instance: “vicinity of deep convection,”

©2014. American Geophysical Union. All Rights Reserved.

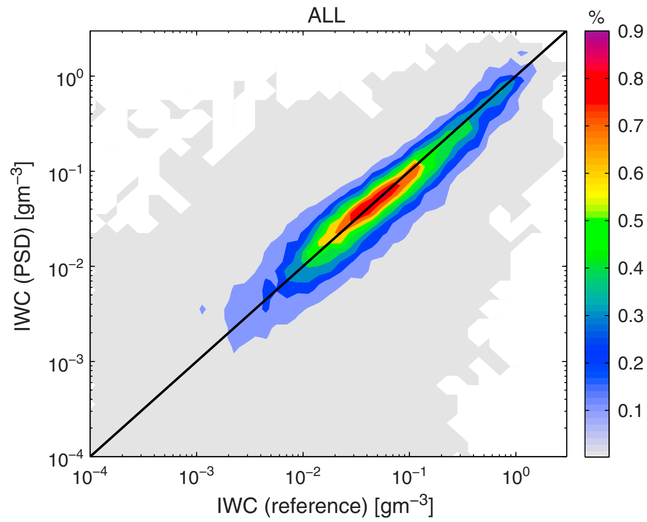

Figure 3. Same as Figure 2 for the whole data set (TC4, NAMMA, CRYSTAL-FACE, ARM, C3VP, AIRS, and Subvisible).

"convectively generated," "warm," or "composite" (including different sort of clouds). The results of the IWC comparison are presented in Figures 2 and 3, which show the probability distribution of the IWC computed using the measured PSD and IWC_{ref} for each campaign and all the campaigns, respectively. Note that we have removed all the data contaminated by liquid water (see section 3.1). It is clearly demonstrated that the mass relationships selected (Table 3) are in good agreement with IWC_{ref}; most of the data are concentrated in the 1:1 region of the scatterplots, and the selected relationships do not seem to introduce any bias in the derived IWC. The best results are obtained for CRYSTAL-FACE and TC4 data, while NAMMA, ARM, and M-PACE values are more scattered. Accordingly, we will use in our calculation the composite $M(D)$ for TC4, ARM, and M-PACE, the relationship obtained for convectively generated cloud for CRYSTAL-FACE, the relationship for clouds in vicinity of deep convection for NAMMA, and the warm cloud relationship for C3VP. Note that the composite relationship is perfectly suitable for at least three campaigns and only CRYSTAL-FACE, NAMMA, and the Subvisible require more specific relationships. We will also compute the visible extinction parameter, and therefore, we also need to be able to derive the cross-sectional area of particles of each given diameter [*Heymsfield et al.*, 2013]. It is directly computed from the projected area of the particle.

The sampled maximum chord length diameter of a given particle is used to define its diameter. The particle "area ratio" is derived from the images areas for each particle normalized by the area of an equivalent diameter circle. Statistics on particle area ratios per size bin are compiled over 5 s intervals. For each size bin and for each 5 s interval, an average area ratio is derived.

Deriving $M(D)$ is clearly an advantage; however, we also need to analyze the impact of commonly used relationships applied to the whole data set. Therefore, we decided to select one of them which is currently used in the radar-lidar DARDAR products (http://www.icare.univ-lille1.fr/projects/dardar/) combining CloudSat and CALIPSO measurements [*Delanoë and Hogan*, 2010]. This is motivated by the fact that the $M(D)$ assumed in the retrieval technique is a combination of two relationships of *Brown and Francis* [1995] for D>300 μm and *Mitchell* [1996] for hexagonal columns. Note that *Brown and Francis* [1995] mass-size relationship has been widely used and evaluated in *Heymsfield et al.* [2010].

Table 3. Mass-Size Relationships Used for Each Campaign

Campaign	Names	Relationships (cgs)
TC4	Composite	$M(D) = 7e^{-3}D^{2.2}$
NAMMA	Vicinity of deep convection	$M(D) = 11e^{-3}D^{2.1}$
CRYSTAL-FACE	Convectively generated	$M(D) = 6.3e^{-3}D^{2.1}$
ARM	Composite	$M(D) = 7e^{-3}D^{2.2}$
M-PACE	Composite	$M(D) = 7e^{-3}D^{2.2}$
C3VP	Warm	$M(D) = 3.59e^{-3}D^{2.1}$
AIRS	Composite	$M(D) = 7e^{-3}D^{2.2}$
Subvisible	Specific	$M(D) = 16.39e^{-3}D^{2.49}$

©2014. American Geophysical Union. All Rights Reserved.

DARDAR mass-size relationships are given below (cgs):

$$M(D) = 1.677\, e^{-1} D^{2.91} \quad D <= 0.01 \text{ cm} \tag{13}$$

$$M(D) = 1.66\, e^{-3} D^{1.91} \quad 0.01 < D <= 0.03 \text{ cm} \tag{14}$$

$$M(D) = 1.9241\, e^{-3} D^{1.9} \quad D > 0.03 \text{ cm} \tag{15}$$

Note that (15) has been modified, assuming an aspect ratio of 0.6 [*Hogan et al.*, 2012] to convert the mean diameter to maximum diameter. This adapted mass-size relationship is used in this study and will be referred to as "DARDAR."

In this study we will compute IWC, N_0^*, D_m, the radar reflectivity factor at 94 GHz (Z), the terminal fall velocity (V_t), and the effective radius (r_e) using the retrieved $M(D)$ and in section 5.4, we will add DARDAR $M(D)$. As a rough approximation, the reflectivity factor can be assumed to be proportional to the sixth moment of the PSD. However, this simplification is not valid at 94 GHz for large particles so the reflectivity is computed using the T-matrix approach, particles are assumed to be spheroids, and the mass-size relationship is used to calculate the fraction of ice included in the spheroid and the dielectric factor. The T-matrix approach requires the knowledge of the aspect ratio of the particles; as a matter of consistency, we assume a ratio of 0.6 [*Hogan et al.*, 2012]. Reflectivity weighted terminal fall velocity is computed using *Heymsfield and Westbrook* [2010]. Note that visible extinction and terminal fall velocity are derived using the particle size distribution and the cross-sectional area of the particles as a function of their diameter. From IWC and the visible extinction, we can compute the effective radius:

$$r_e = \frac{3}{2} \frac{\text{IWC}}{\sigma \rho_i}, \tag{16}$$

where ρ_i is the density of solid ice and σ is the visible extinction *Foot* [1988].

4. Impact of the Normalization

4.1. Impact on the PSD

PSDs from each field campaign are derived in term of equivalent melted diameter using equation (1) and the mass-size relationship identified earlier (section 3.3), and for each spectrum, N_0^* and D_m are also computed. Figure 4 shows the impact of the normalization, where contours illustrate the distribution of the data in both configurations: raw (left) and normalized (right) spectra. The impact of the normalization is obvious, data are concentrated in a smaller area, and sampling effects are reduced. NAMMA and CRYSTAL-FACE non-normalized spectra exhibit a large scatter with several orders of magnitude in concentration for a given diameter. This is probably due to the fact that the data are sampled in convectively generated ice clouds. The maximum number of hits is about 0.4–0.5% while the maximum of data, once normalized, reaches more than 1.2% and spans only a few orders of magnitude in concentration for a given D_{eq}/D_m.

The raw TC4, ARM, M-PACE, C3VP, and AIRS spectra, despite a wide range of values in number concentration, show green peaks (0.5%) at around 10^2 m^{-3}µm^{-1}, but the variability in concentration clearly decreases after normalization. Subvisible data span a smaller range of diameters; this is expected due to the very cold temperatures and the nature of the sampled clouds. The raw concentration remains largely variable (i.e., several orders of magnitude), and the impact of the normalization is noticeable.

The effect of the normalization is important for each spectrum, while the raw spectra had different patterns and differences in the distribution of the concentration the normalized spectra show very similar shapes. Most of the data are concentrated in the area where $D_{eq}/D_m = 1$, even for Subvisible data, and normalized PSDs will differ from their wings around this value. *Delanoë et al.* [2005] and *Field et al.* [2007] showed that as a function of the field campaign location, the shape of the normalized PSD was different and implied differences in cloud processes. This scaling effect is due to the way D_{eq} is distributed around the volume-weighted diameter value. As shown in Figure 5, the distribution of D_m is linked to the shape of the normalized PSD. For monomodal and peaked distributions as in TC4, NAMMA, and ARM, the normalized PSDs show a "bell" shape (less values for small D_{eq}/D_m and a narrower distribution) while CRYSTAL-FACE has a rather flat distribution. The latter exhibits two peaks in the D_m distribution, one around 180 µm and another one for larger particles around 600 µm. This remark concerning the monomodal of multimodal characteristics could also be made for N_0^* distribution (Figure 5) although it is not as clear as for the normalized diameter axis. As was mentioned in *Delanoë et al.* [2005], we have a correlation between N_0^* and D_m and this result is not surprising.

©2014. American Geophysical Union. All Rights Reserved.

10.1002/2013JD020700

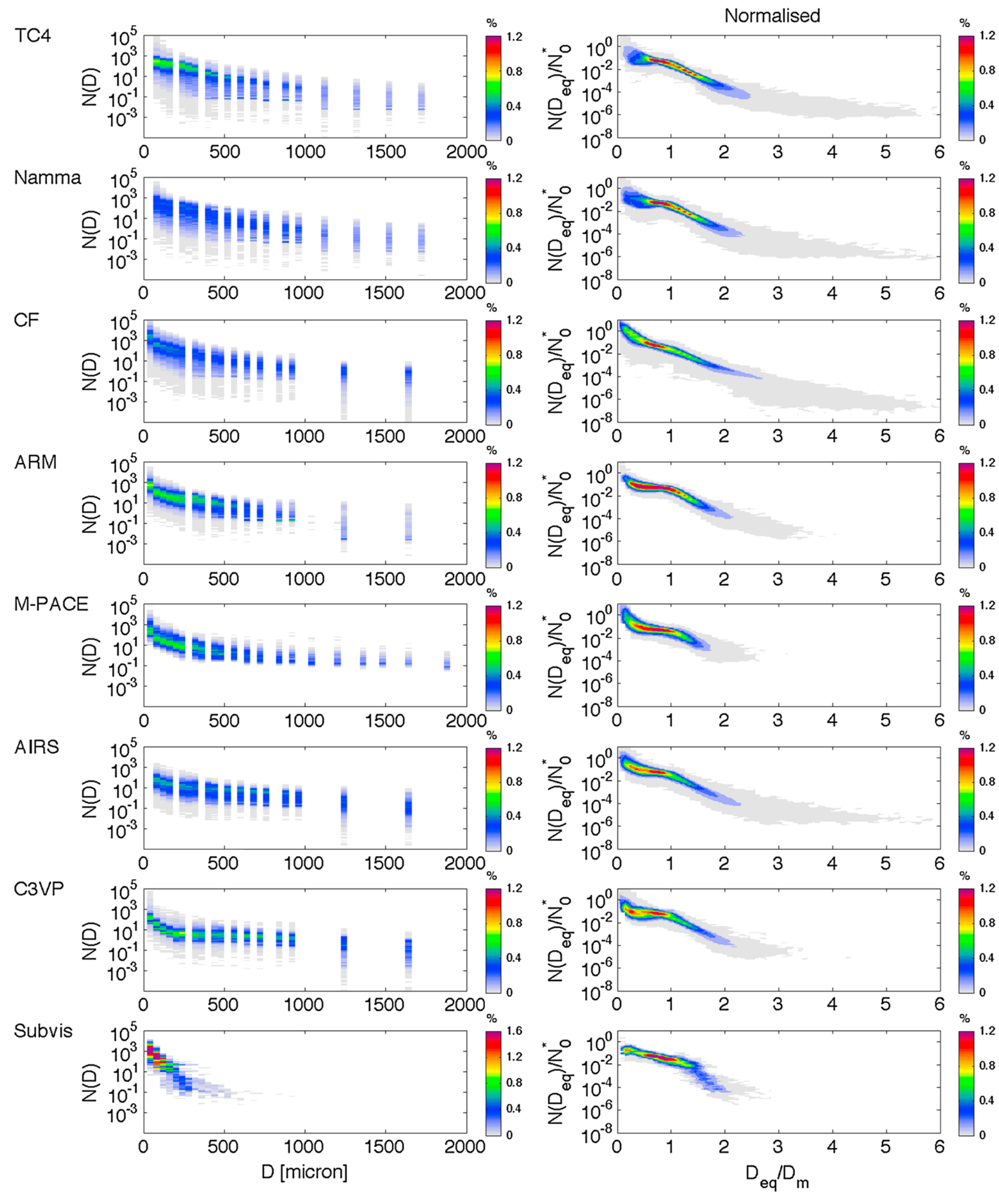

Figure 4. Impact of the normalization approach on the particle size distribution for each field campaign. (left) The PSDs before normalization. (right) The effects of the normalization. Note that the normalized PSD is defined as a function of the equivalent melted diameter.

The most important result is the much lower scatter of concentrations for any diameter when the distributions have been normalized. Spaceborne remote sensing retrieval algorithms need to use parameterizations of PSDs and which can be very difficult to adapt to specific local cloud conditions. The idea, here, is to provide a single parameterization, and all the data are grouped in a unique data set in Figure 6. The effect of the normalization is even more noticeable compared with one single campaign as several ice cloud types (convectively or synoptically generated) are all combined. Note that the zeros included in the distribution are not represented in this graphic as we are using a log scale.

4.2. Link Between Temperature and PSD Shape

We saw in the previous section that the shape F of the normalized PSD was dependent on D_m and N_0^* distributions. The link between temperature and the shape of the normalized PSD is investigated in Figure 7. The data set has been split into eight intervals between -80°C and 0°C, and the results are shown in Figures 7a to 7h. While the temperature clearly has an impact on the normalized PSD, it remains difficult to claim that there is a linear relationship between the intensification of the bell shape and temperature and a robust

©2014. American Geophysical Union. All Rights Reserved.

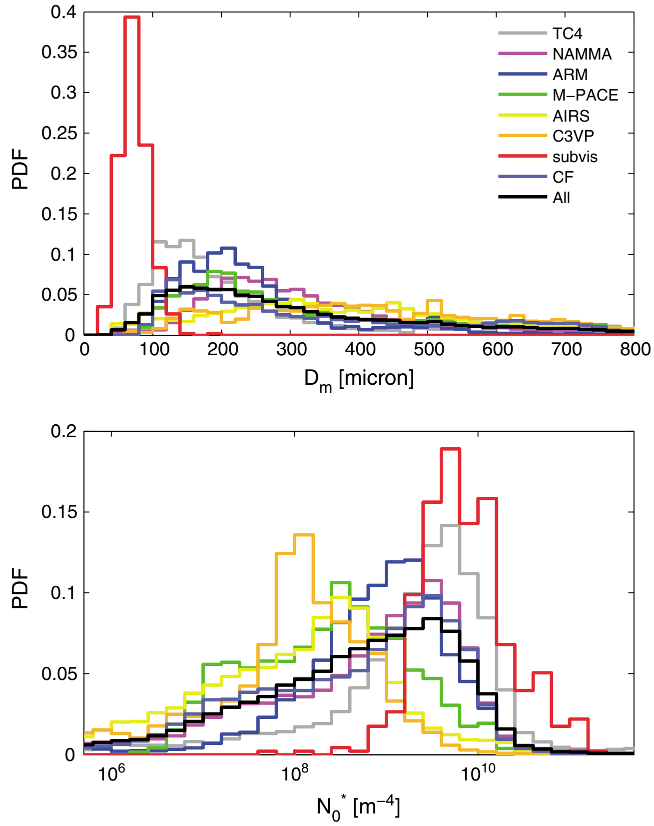

Figure 5. PDFs of (top) D_m and (bottom) N_0^*.

parameterization cannot be derived. However, we observe that as the temperatures get lower, the data get more concentrated around the $D_{eq}/D_m = 1$ area. For very cold temperatures (Figures 7g and 7h), the tails of the normalized PSD shape ($D_{eq}/D_m > 2$) have vanished.

These results are corroborated by Figures 7i and 7j which represent D_m and N_0^* distribution, respectively. We clearly observe narrow distributions of D_m for cold temperatures, but this is not obvious for N_0^* as its distribution at −65°C appears broader than for warmer temperatures (below −35°C). Such a result would imply

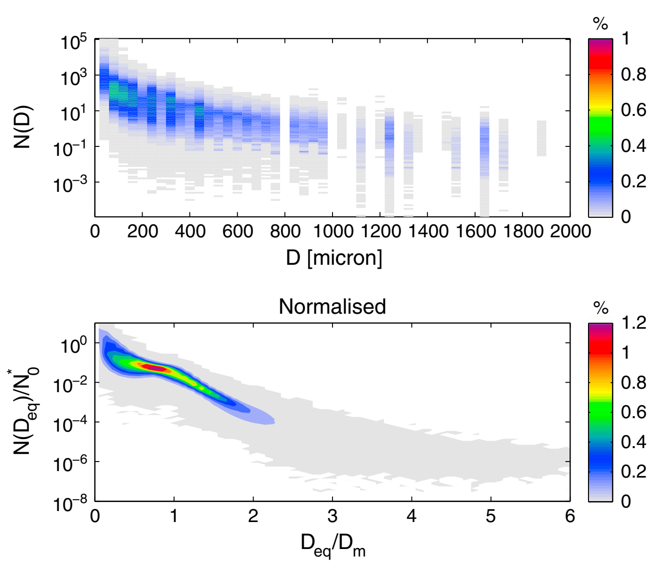

Figure 6. Impact of the normalization approach on the particle size distribution for full data set.

©2014. American Geophysical Union. All Rights Reserved.

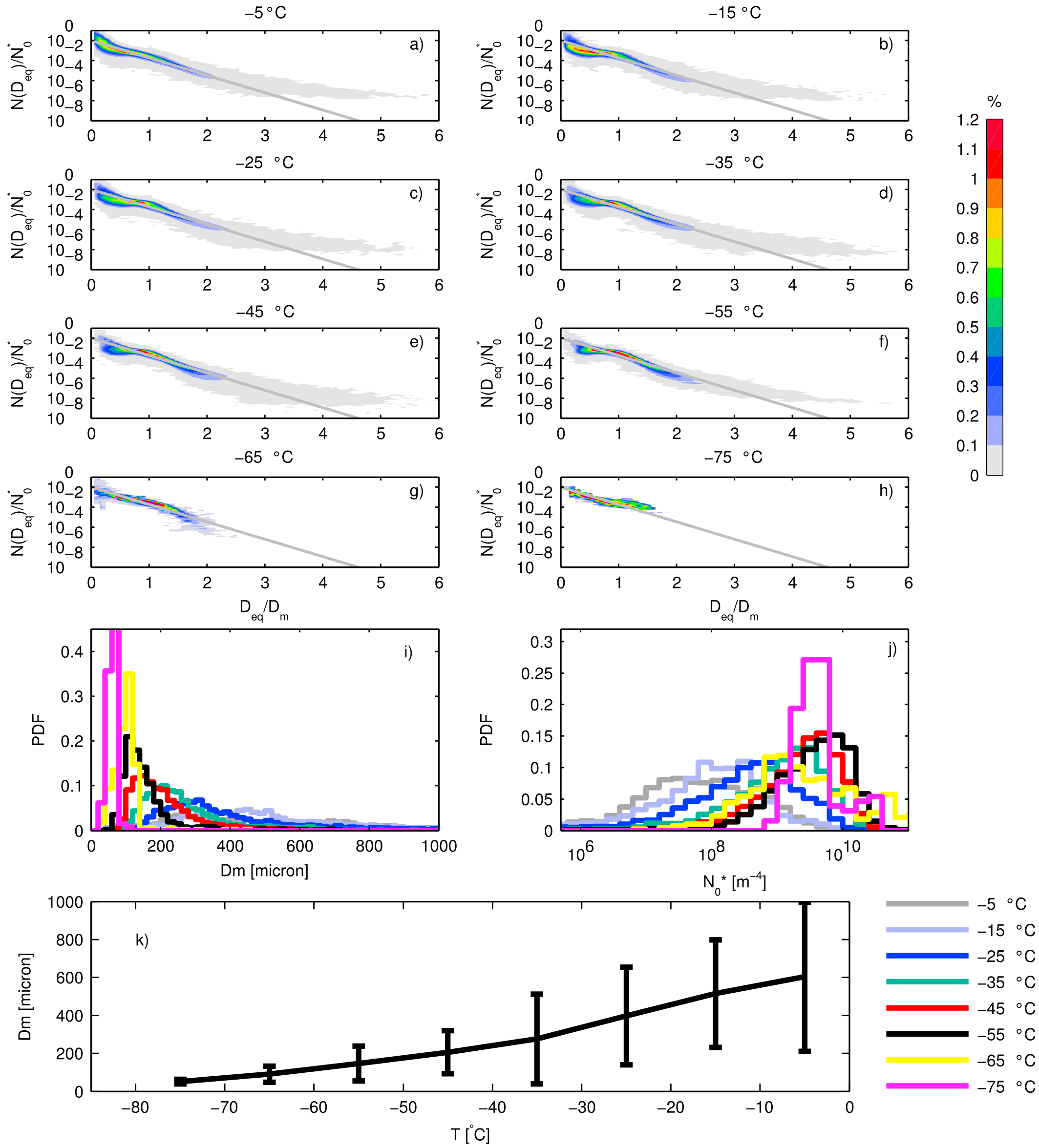

Figure 7. (a–k) Particle size distribution for different temperature ranges. These plots include all data. Grey line represents an exponential function.

that it is possible to have a slightly different behavior between D_m and N_0^* distributions. We will come back to these results later in section 6.2. Figure 7k shows the relationship between D_m and the temperature. Once again, the smallest values are observed for cold temperatures and the largest values are observed when we get closer to the freezing level. Another very interesting result is the increase in the variability around the mean value when temperatures get warmer. When temperatures increase, the range of diameters increases as we can have ice particles coming from different microphysical processes with an increasing role played by the aggregation process.

4.3. Impact of the Normalization on the Moments of the PSD

Cloud variables (IWC, visible extinction, and effective radius) and observed parameters can be expressed as moments of the PSD. We can therefore envisage expressing each moment as a function of D_m and N_0^*. Figure 8 shows the results of the normalization on the IWC, extinction, and reflectivity. Figure 8a exhibits IWC as a function of D_m and Figure 8b IWC divided by N_0^* in log space. This is an expected result as D_m, IWC, and N_0^* are linked by equation (9). One of the objectives of the normalization approach is to allow for

©2014. American Geophysical Union. All Rights Reserved.

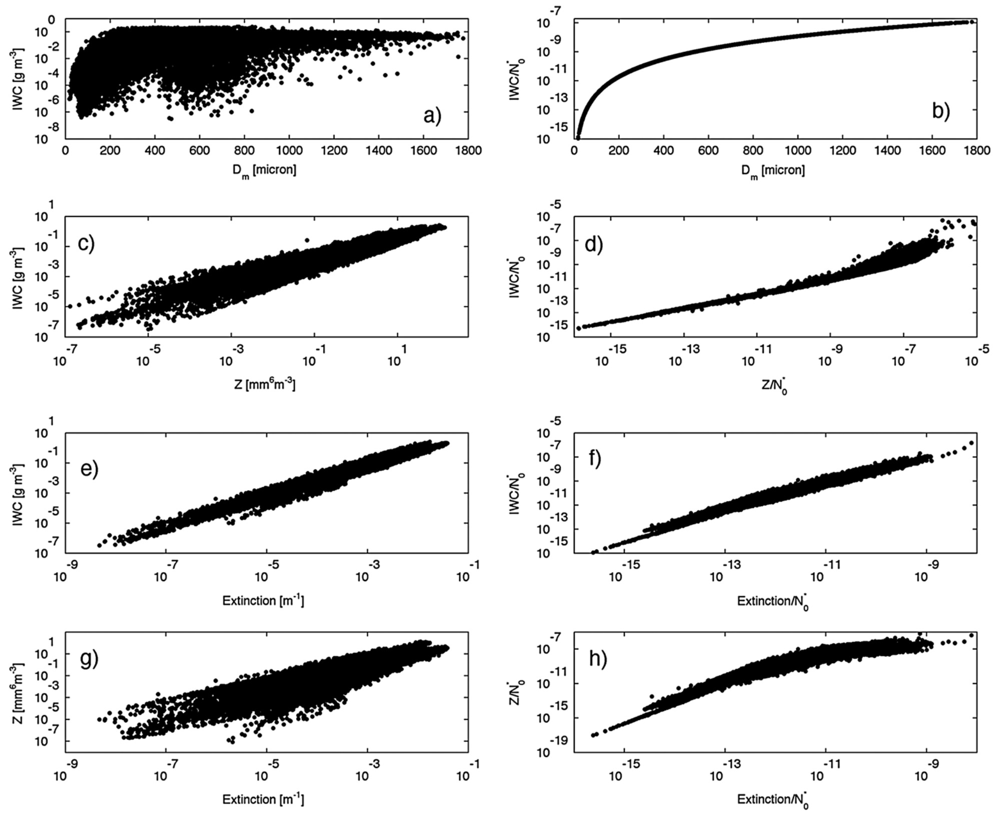

Figure 8. Impact of the normalization on different moments of the particle size distribution. (a, c, e, and g) IWC-D_m, IWC-Z, IWC-extinction, and Z-extinction relationships, respectively. (b, d, f, and h) The result of the normalization for each relationship.

the development of lookup tables linking the observations (Z, σ from lidar backscatter) to cloud properties which are used in many retrieval techniques. The normalization by N_0^* reduces the scatter as shown by Figures 8b–8d, 8f, and 8h which represent IWC-Z, IWC/N_0^*-Z/N_0^*, IWC-extinction, IWC/N_0^*-extinction/N_0^*, and Z-extinction, Z/N_0^*-extinction/N_0^* relationships, respectively. In this situation, some of the variability is incorporated in N_0^* and implies that it can be used a as common denominator for cloud and observed variables [*Delanoë et al.*, 2007; *Delanoë and Hogan*, 2008]. As a result, using equation (12), it is possible to build lookup tables linking D_m to all normalized parameters (IWC/N_0^*, extinction/N_0^*, Z/N_0^*). Note that r_e and V_t do not need to be normalized as they are independent of N_0^*. If we assume a single normalized PSD shape for all ice clouds, it is therefore not necessary to fit the relationships between cloud variables. The main advantage in using the normalization approach versus a basic fit (between variables) is the resulting consistency in the relationship between different PSD moments. For instance, if we have two independent measurements (Z and visible extinction) and we want to retrieve the PSD, it is possible. IWC, Z, and the visible extinction are all linked by N_0^* and D_m. The remaining scatter obtained after normalization actually reflects the natural variability of the normalized PSD shape and the assumption of a single $M(D)$.

In order to use equation (12), it is necessary to obtain the best coefficients (α and β) to represent the normalized PSD. It is the aim of next section.

5. Best Parameterization for the Normalized PSD

5.1. Approach Used

Delanoë et al. [2005] showed that it was possible to represent the normalized PSD using the modified gamma function represented by equation (12). Several pairs of coefficients (α and β) were used to estimate the optimal representation. In this paper we use a slightly different approach; the optimal coefficients are derived using a least square regression linear fit on moments of the PSD as proposed by *Field et al.* [2005, 2007]. The main difference here is that we are using several combinations of moments to get the optimal

©2014. American Geophysical Union. All Rights Reserved.

Table 4. Optimal Coefficients for the Modified Gamma for Each Campaign[a]

Moments	Ext-Z		Ext		Z	
Campaigns	α_{PSD}	β_{PSD}	α_{PSD}	β_{PSD}	α_{PSD}	β_{PSD}
TC4	−0.113	1.765	−0.435	2.126	−0.193	1.798
NAMMA	−0.391	1.737	−1.466	4.912	−0.189	1.645
CRYSTAL-FACE	−0.442	1.557	−0.888	3.980	−1.765	2.518
ARM	−0.085	2.100	−0.978	2.639	−0.059	2.168
M-PACE	−1.948	8.798	−0.069	1.567	−2.187	12.477
C3VP	0.024	2.114	−1.122	8.620	8.817	0.599
AIRS	−0.055	1.689	−1.386	8.216	−0.013	1.630
Subvisible	−1.463	3.105	−1.899	6.600	−0.158	1.792
All	−0.262	1.754	−1.254	4.189	−0.234	1.709
All (DARDAR)	−0.237	1.839	−0.044	1.633	−0.189	1.827

[a] Extinction and/or reflectivity has been used to fit the theoretical shape.

(α, β) pair. For instance, we use a low moment of the PSD, the visible extinction, and the reflectivity factor a high moment of the PSD. The best coefficients, α and β, are obtained by minimizing the cost function J:

$$J = \sum^{n} \left[\left(1 - \frac{\text{ext}_{\text{norm}}(\alpha, \beta)}{\text{ext}_{\text{true}}} \right)^2 + \left(1 - \frac{Z_{\text{norm}}(\alpha, \beta)}{Z_{\text{true}}} \right)^2 \right], \tag{17}$$

where n is the number of component PSDs, ext_{true} and Z_{true} are the extinction and the reflectivity computed using the measured PSD, and ext_{norm} and Z_{norm} are derived using the normalized PSD. Note that we actually minimize the ratio between the normalized PSD and the true PSD, aiming to avoid imbalance between the contribution of the two moments in the cost function. It is also possible to use only one of the moments for the minimization. Extinction and reflectivity are computed using the normalized PSD shape using the measured area and mass-size relationships D_m and N_0^* derived from the measured PSD.

5.2. Coefficients of the Analytical Normalized PSD

The best analytical normalized PSD coefficients (α and β) are summarized in Table 4, using extinction and/or reflectivity as noted above.

Figure 9 illustrates the results in terms of PSD shape for each campaign and for all campaigns combined. Figures 9a–9c represent the parameterized PSD when extinction and/or reflectivity is used in the minimization process, respectively. Figure 9d shows β coefficients as a function of α coefficients. Except for the M-PACE campaign (using extinction-Z couple and Z only), the shapes are very similar in the range $0.5 < D_{eq}/D_m < 1.5$ where the data are concentrated. This result is consistent with Figure 4, and differences are observed for the wings of the distribution. However, it is obvious that the choice of the moment to fit the PSD is crucial. A low-order moment is mainly weighted by the small particles while a high-order moment is weighted by large particles. For this reason the ability of the normalized PSD to represent small or large particles depends on the pair of coefficients. This is why we suggest using visible extinction and reflectivity to derive those coefficients.

The tail of the distribution is strongly constrained by the reflectivity while the shape of the distribution for small normalized diameters is driven the extinction. When normalizing the PSD, this relationship is not as straightforward, as small and large particles are spanning the whole D_{eq}/D_m range.

5.3. Impact of the Normalized Coefficient on the Cloud Variables and the Radar Measurements

In the previous section, we saw the impact of the derived coefficients on the normalized PSD shape. In this section we show the impact of the normalized PSD shape on cloud and observed variables. Therefore, visible extinction, effective radius, reflectivity, and terminal fall velocity are computed using the observed PSD and the derived mass-size relationships and they are compared to those obtained using the analytical shape and the retrieved α and β. It is important to note that we do not have to evaluate the impact of the normalized PSD on IWC as it is directly computed from N_0^* and D_m.

 ©2014. American Geophysical Union. All Rights Reserved.

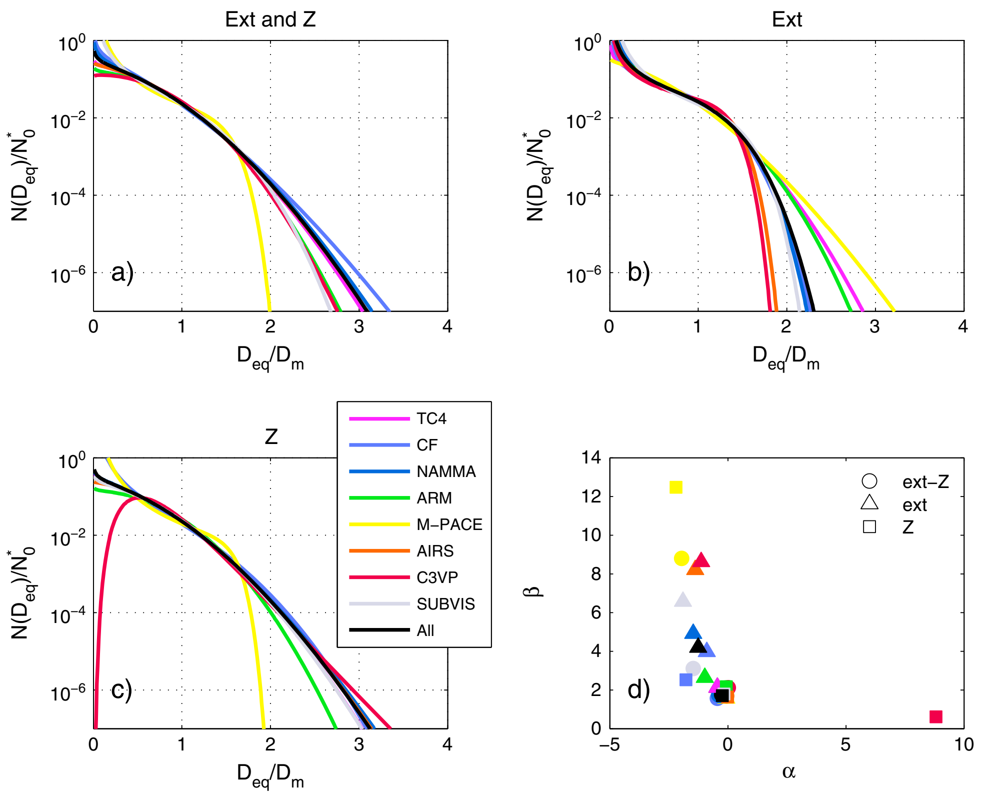

Figure 9. Idealized representation of the normalized PSD (modified gamma shape) for each data set, obtained after minimization using (a) extinction and reflectivity, (b) extinction alone, and (c) reflectivity factor alone. Coefficients of the modified gamma shapes can be found in Table 4 and are represented in panel (d).

Figure 10 summarizes the relative mean difference and the standard deviation between the measured PSD and the analytical shape. The full description of Figure 10 is given in the caption. The mass-size relationships, used for the calculations, have been retrieved using the PSD and the direct measurements of IWC. The corresponding $M(D)$ will be referred to as the "retrieved" $M(D)$. Note that we actually compare the normalized parameters (i.e., independent of N_0^*) but this is strictly equivalent to comparing the unnormalized parameters as N_0^* cancels out when we compute the ratio. The pairs of coefficients used for computing the analytical PSD are those presented in the previous section and summarized in Table 4. The most important result here is that the pair of coefficients derived using the full data set gives very similar results to the pairs of coefficients derived for each campaign. The bottom panel also shows the distribution of each cloud variable or radar measurement (extinction, effective radius, radar reflectivity, and terminal fall velocity), which indicates where it is most important to have the smallest differences.

1. The relative mean difference for visible extinction (Figures 10a, 10e, and 10j) is between −10% and 10% where most of the data are concentrated, i.e., where visible extinction is greater than 1 $e^{-5}m^{-1}$ (Figure 10n). This is verified independently on the constraint (i.e., Z only, Z and extinction, or extinction only), which is used to retrieve the pair of coefficients. As expected, for the small extinction values (i.e., less than 5 e^{-4} m^{-1}), the lowest relative mean difference for extinction is obtained when visible extinction is used as a constraint to fit the analytical PSD shape. In this configuration, we observed the lowest difference variability; the envelope (i.e., ± standard deviation) belongs to the [−15%, 15%] interval. The envelope shown for the full data set pair of coefficients (red one) is narrower than for the "campaign" pair of coefficients (black one) when Z is used as the only constraint (Figure 10j). This is not surprising due to the difference in the order of the moments. However, the relative mean difference is slightly closer to zero for large extinctions (larger than 5 e^{-4} m^{-1}) when Z is the only constraint.
2. The relative mean difference for r_e (Figures 10b, 10f, and 10k) is consistent with the relative mean difference for visible extinction with values within the [−10% 10%] range. This is an expected result as r_e is a combination of IWC and visible extinction (equation (16)) and IWC/N_0^* is an analytical function of D_m.

©2014. American Geophysical Union. All Rights Reserved.

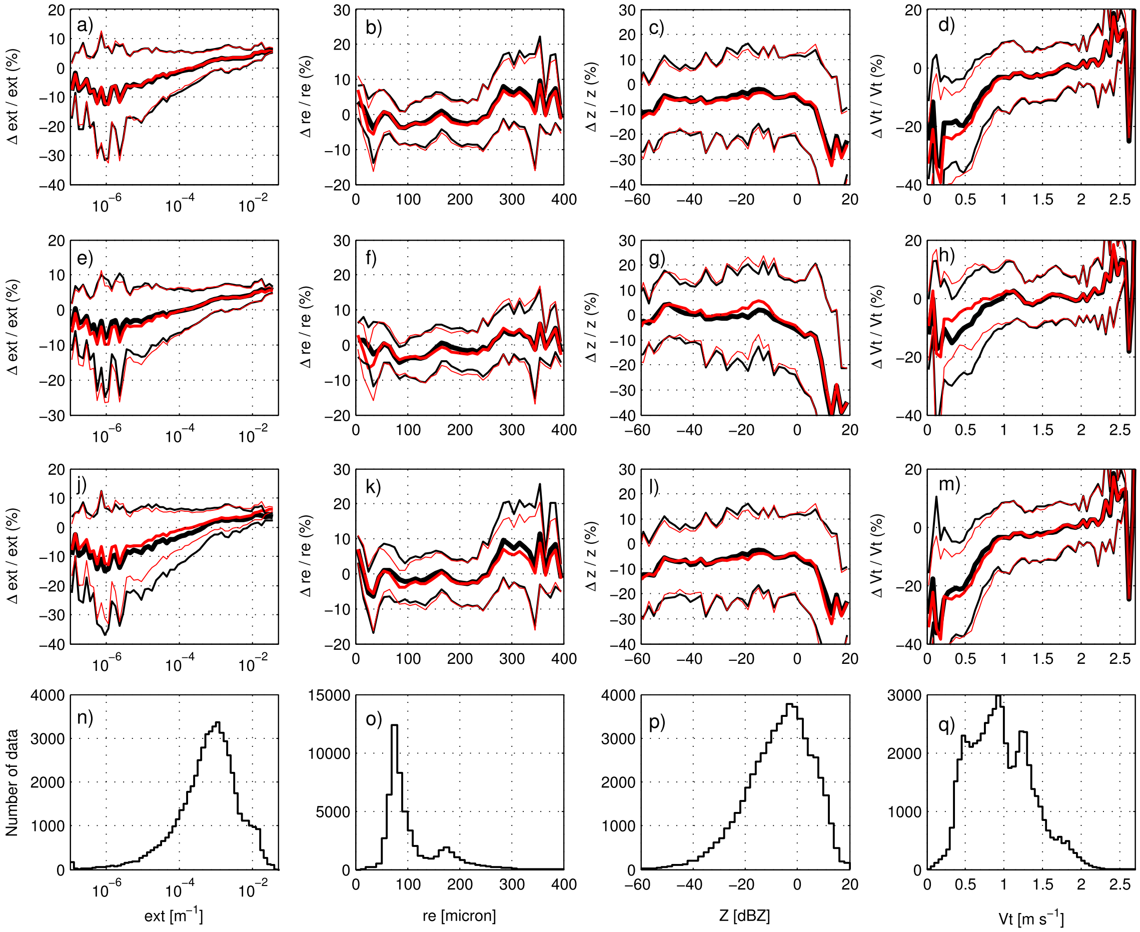

Figure 10. Relative mean difference (in percent) between (a, e, and j) extinction, (b, f, and k) r_e, (c, g, and l) Z, and (d, h, and m) V_t computed with the analytical gamma shape and the measured PSD. α and β coefficients which are used to compute cloud and observed variables are obtained using different constraints (Figures 10a–10d: Z and extinction; Figures 10e–10h: only extinction; Figures 10j–10m: only Z). Black lines represent variables retrieved using the best α and β coefficients for each campaign while red lines correspond to variables computed with coefficients derived from the full data set. Thickest lines are the mean values and thinnest lines represent the envelopes (mean ± standard deviation.) Figures 10n–10q illustrate the number of data points used to compute the mean values. The retrieved $M(D)$ is assumed.

3. Figures 10c and 10l show that the relative mean difference for Z is around −10% when Z is used as constraint. This difference seems to be smaller if extinction is used (Figure 10g), within average less than a few percent. However, the absolute relative mean difference strongly increases for large values of reflectivity, i.e., $Z > 10$dBZ. The relative standard deviations are about 15%–20% for the three presented configurations.
4. The absolute relative mean difference for V_t (reflectivity weighted terminal fall velocity) exhibits different results compared to other variables. When V_t is less than 0.5 m s^{-1}, it can exceed 20% if we use a pair of coefficients derived using Z. It does not exceed 10% when $V_t > 0.7$ m s^{-1}.

We can conclude that for the visible extinction, r_e, Z, and V_t, the absolute relative mean difference is approximatively 10% if we use the full data set α and β coefficients. These results are consistent with *Delanoë et al.* [2005].

5.4. Impact of the Mass-Size Relationship on the Normalized PSD

In satellite retrieval techniques, it is common to use a single mass-size relationship (or a combination) as it remains difficult to adjust $M(D)$ due to a lack of independent measurements. Our objective in this section is to assess whether the mass-size relationship choice is crucial in the characterization of the analytical normalized PSD. We also propose to quantify the error made if we use a more commonly used mass-size relationship instead of the retrieved $M(D)$ in the cloud and observed variables computed using the analytical normalized PSD shape.

©2014. American Geophysical Union. All Rights Reserved.

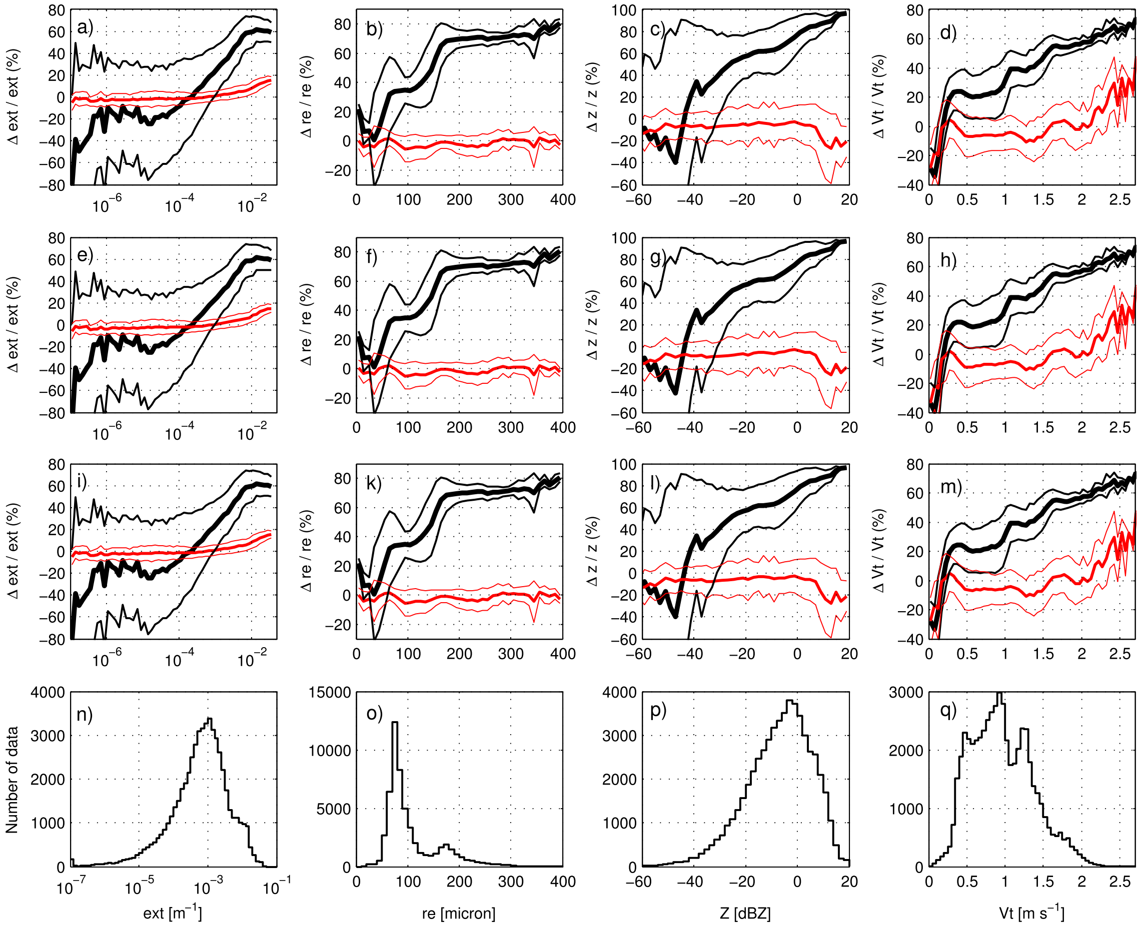

Figure 11. Same as Figure 10 but DARDAR $M(D)$ is assumed. See text for details or color significations.

The first step is to retrieve α and β coefficients with the same mass-size assumption as the DARDAR product (see section 3.3). Those coefficients can be found in Table 4 and are referred to as DARDAR. Figure 11 is the same as Figure 10, where red color is attributed to the relative mean difference (and standard deviation) between cloud and observed variables computed with the analytical normalized PSD and the observed PSD assuming DARDAR $M(D)$. Black lines are the relative mean difference (and standard deviation) between cloud and observed variables computed with the analytical normalized PSD assuming DARDAR $M(D)$ and the observed PSD using the retrieved $M(D)$. In the next section, it will be referred as the relative mean difference between the DARDAR and the observed PSD. From this figure we can conclude that the impact of the choice of $M(D)$ is very large compared to the choice of α and β coefficients. This is a strong result regarding the normalization approach.

As shown in Figures 11a–11m, the error (including bias and variability) due to the use of the normalized approach, when we assume the same mass-size relationship (red curves), is considerably smaller than the error due the $M(D)$ assumption (black curves). This statement is valid for both cloud (extinction, effective radius) and measurement parameters (V_t, Z). We also see that relative mean difference and relative standard deviation values strongly vary with the assessed variable range, for instance the relative mean difference in Z goes from −50% for reflectivity below −40 dBZ to 95% for high reflectivity (Figures 11c, 11g, and 11i).

6. Parameterization for Key Ice Cloud Parameters

We demonstrated the impact of using the normalized PSD and showed that it could be represented by an analytical function. As a result, if we can retrieve N_0^* and D_m, it is therefore possible to approximate the particle size distribution ($N(D_{eq}) = N_0^* F_{\alpha,\beta}(D_{eq}/D_m)$). However, one of the two moments is sometimes missing or cannot be retrieved due to an insufficient number of constraints in a retrieval process (like radar-only and

 ©2014. American Geophysical Union. All Rights Reserved.

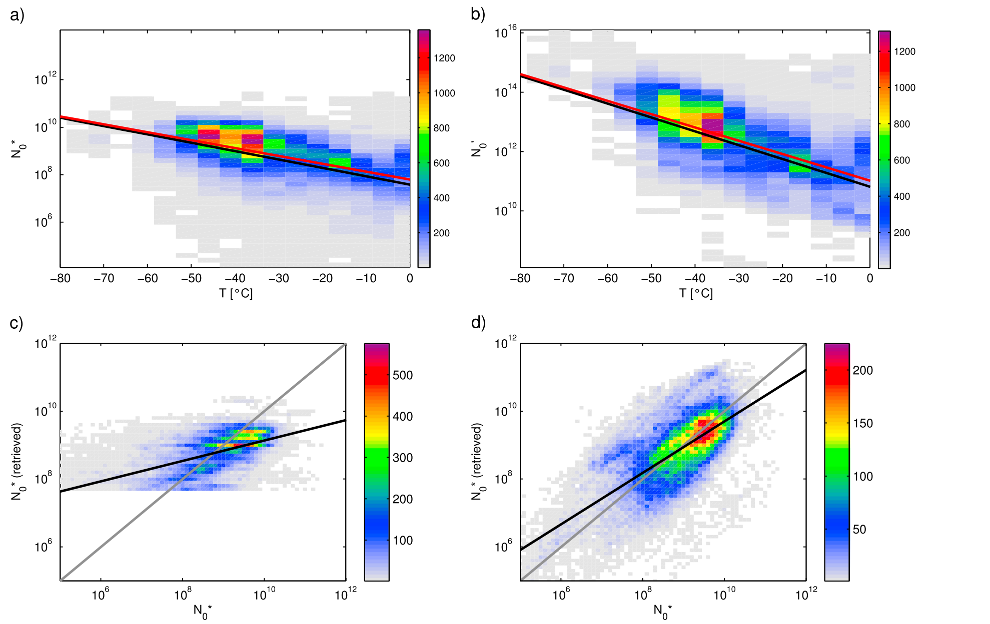

Figure 12. A priori values for N_0^* and N_0'. (a) N_0^* computed using measured PSD and retrieved $M(D)$ as a function of temperature. The black line is the corresponding parameterization. (b) N_0' as a function of temperature. The red lines are the parameterizations for DARDAR $M(D)$. (c, d) Retrieved N_0^*, using N_0^* and N_0' temperature parameterizations (retrieved $M(D)$ only), respectively. Color contours show the number of data in Figures 12a–12d.

lidar-only retrievals for instance, where only one constraint is available and a parameterization of one of those two scaling parameters is needed). Some moments of the PSD, such as V_t, do not depend on N_0^*, and consequently, we will retrieve D_m using the radar Doppler velocity [*Delanoë et al.*, 2005, 2007]. Therefore, in the next section we investigate different possible options to parameterize N_0^* using either temperature or D_m.

6.1. An A Priori for N_0^* and N_0'

Delanoë and Hogan [2008] showed that there was a clear temperature dependence of N_0^* but that the derived relationship was strongly dependent on the IWC. Note that in this previous study, bulk measurements of IWC were not available and the mass-size relationship used was that from *Brown and Francis* [1995]. Figure 12a shows the relationship between N_0^* and temperature using the retrieved $M(D)$ and the measured PSD. The black line represents the corresponding parameterization and is expressed as

$$\ln(N_0^*) = A_{1N_0^*} T + A_{2N_0^*}, \tag{18}$$

where $A_{1N_0^*}$ and $A_{2N_0^*}$ coefficients can be found in Table 5, T is the temperature in degrees Celsius, and N_0^* is in m^{-4}. The red line illustrates the relationship obtained if we use the measured PSD and the DARDAR mass-size relationship. The coefficients $A_{1N_0^*}$ and $A_{2N_0^*}$ corresponding are also presented in Table 5. Both relationships are very similar; this is an expected result as the DARDAR N_0^* is on average 1.4 time N_0^* with the measured $M(D)$. Therefore, the change appears very small in log space.

Figure 12c compares N_0^* obtained from the measured PSD (x axis) against the one computed using the parameterization (y axis). We can see that the parameterization does not capture the variability of N_0^*. The retrieved values are confined between about 10^8 and 10^{10} m^{-4}. The difficulty in representing the extreme

Table 5. $N_0^*(T)$ and $N_0'(T)$ Parameterization Coefficients

	$N_0^*(T)$			$N_0'(T)$	
Mass-Size Relationship	$A_{1N_0^*}$	$A_{2N_0^*}$	n	$A_{1N_0'}$	$A_{2N_0'}$
Retrieved relationships [*Heymsfield et al.*, 2010]	−0.081014	17.469	1.1	−0.10757	24.9
DARDAR	−0.076586	17.948	1.1	−0.10325	25.37

©2014. American Geophysical Union. All Rights Reserved.

values of N_0^* can be a problem for establishing our a priori information. As a result, *Delanoë and Hogan* [2008] proposed to use a new variable N_0' which depends on N_0^* and visible extinction:

$$N_0' = N_0^*/\sigma^n. \tag{19}$$

where σ is the visible extinction per meter and n a coefficient which can be adjusted.

This choice was driven by the idea of using a variable which is very well constrained by the lidar measurement.

The parameterization as a function of temperature is the following:

$$\ln(N_0^*/\sigma^n) = A_{1N_0'}T + A_{2N_0'} \tag{20}$$

where T is the temperature in degrees Celsius and $A_{1N_0'}$, $A_{2N_0'}$, and n are in Table 5. By minimizing the least square sense the difference between N_0^* and the retrieved values using equation (20), n, $A_{1N_0'}$, and $A_{2N_0'}$ are obtained.

Figure 12b represents the N_0' variable as a function of temperature using $n = 1.1$. Both parameterizations using measured $M(D)$ and DARDAR are plotted on the contour representation. As it was the case for coefficients $A_{1N_0^*}$ and $A_{2N_0^*}$, $A_{1N_0'}$ and $A_{2N_0'}$ coefficients are similar for the retrieved $M(D)$ and DARDAR. Note that extinction which is used to derive the relationships is directly computed from area dimensional probes measurements. As shown in Table 5, n coefficients for the retrieved $M(D)$ and DARDAR are very close to 1. This result implies that the σ/N_0^* ratio would also be a good candidate for the a priori information. The slight difference is certainly due to the fact that we use an extinction directly derived from the probes and not from a simple parameterization. However, the n coefficient differs from the one proposed in *Delanoë and Hogan* [2008] ($n = 0.6$). This is due to the choice of the mass-size and area-size relationships assumed to calculate extinction and the moments of the PSD.

Figure 12d illustrates the result of applying the parameterization obtained for the measured $M(D)$. We clearly see that dividing N_0^* by a power of extinction allows us to derive a parameterization valid for whole range of N_0^*. This is a striking result compared to the simple $N_0^*(T)$ parameterization. An error assessment, not shown here, has been carried out and showed that for both parameterizations the mean relative error on N_0^* exceeds 200%. As N_0^* is not a real cloud variable, we propose to evaluate the error of both parameterizations on IWC. To do so we first derive a parameterization of IWC as a function of N_0^* and Z and then use the $N_0^*(T)$ and $N_0'(T)$ to calculate N_0^*.

Figure 13 is a contour plot of the IWC$/N_0^*$ as a function of Z/N_0^*. As mentioned in section 4.3, the impact of the normalization is obvious. We can distinguish two areas. The first one shows a linear variation between the logarithm of IWC$/N_0^*$ and Z/N_0^*, which corresponds to the Rayleigh regime region (particle size is small enough with respect to the radar wavelength) when $\frac{Z}{N_0^*} \leq 10^{-10}$ mm^6m. The second area, when $\frac{Z}{N_0^*} > 10^{-10}$ mm^6 m shows the Mie effects and the reflectivity cannot be approximated by the sixth moment of the PSD anymore. Taking this into account, we derive, depending on the Rayleigh/Mie regime, two different parameterizations:

when $\frac{Z}{N_0^*} \leq 10^{-10}$ mm^6m

$$\log_{10}\left(\frac{\mathrm{IWC}}{N_0^*}\right) = 0.5787\log_{10}\left(\frac{Z}{N_0^*}\right) - 4.8923 \tag{21}$$

and when $\frac{Z}{N_0^*} > 10^{-10}$ mm^6m

$$\log_{10}\left(\frac{IWC}{N_0^*}\right) = 0.0258\log_{10}\left(\frac{Z}{N_0^*}\right)^3 + 0.7629\log_{10}\left(\frac{Z}{N_0^*}\right)^2 + 8.1496\log_{10}\left(\frac{Z}{N_0^*}\right) + 20.3024 \tag{22}$$

where Z is in mm$^6m^{-3}$, N_0^* in m^{-4}, and IWC in g m^{-3}.

The two relationships are represented by the red curve in Figure 13. Note that we constrained the relationships in a way that we avoid any discontinuity between the two regimes. In Figure 14 we present the impact of using $N_0^*(T)$ or $N_0'(T)$ in the IWC$/N_0^*$- Z/N_0^* relationship. Figure 14a corresponds to a scatterplot between the measured IWC and the parameterized IWC using $N_0^*(T)$ relationship. Figure 14b is similar to Figure 14a

©2014. American Geophysical Union. All Rights Reserved.

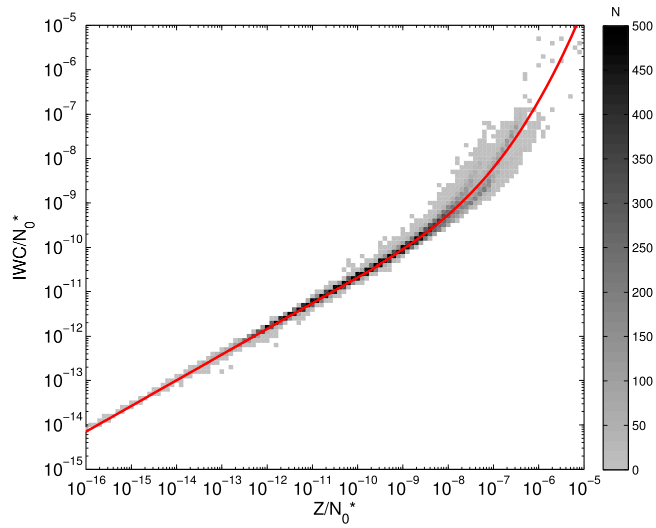

Figure 13. Relationship between normalized IWC and Z in log space. The filled contours show the number of points. The red curve represents a parameterization of the relationship, combining a linear function for the Rayleigh regime part and cubic function when the Rayleigh approximation is not applicable. The relationships are given in the text.

but for $N_0'(T)$ parameterization. For the latter we have used the measured extinction. Note that this extinction could be provided by lidar measurements in a retrieval technique context. From these two panels, we can see that the $N_0'(T)$ parameterization gives better results and the scatterplot is closer to the 1:1 line than the $N_0^*(T)$ relationship. This result is confirmed by Figure 14c. It shows the mean relative difference between the retrieved IWC and the measured IWC as a function of the measured IWC. For large IWC (i.e., IWC > 0.01 g m^{-3}), the $N_0^*(T)$ relationship gives good results with a mean relative difference within the range

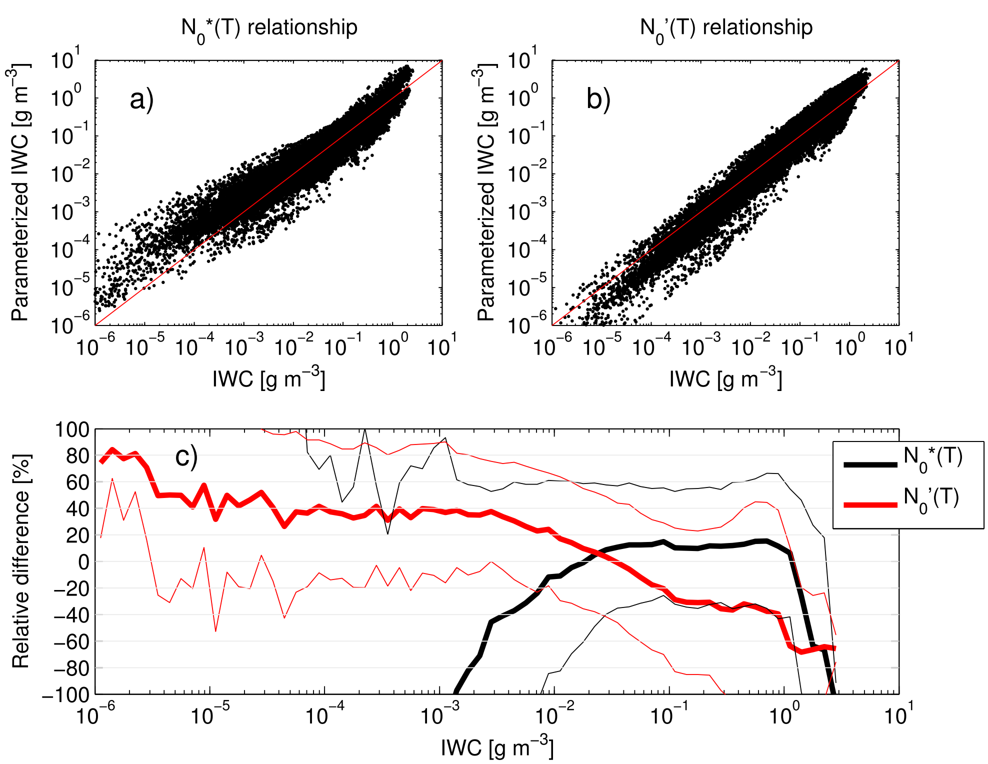

Figure 14. Impact of the $N_0^*(T)$ and $N_0'(T)$ relationships on the retrieval of IWC using the IWC/N_0^*-Z/N_0^* relationship presented in Figure 13. (a, b) Scatterplots of parameterized IWC versus measured IWC. (c) The mean relative difference (thick lines) and its envelope (thin lines) between measured and parameterized IWC: black lines for the $N_0^*(T)$ and red lines for $N_0'(T)$.

©2014. American Geophysical Union. All Rights Reserved.

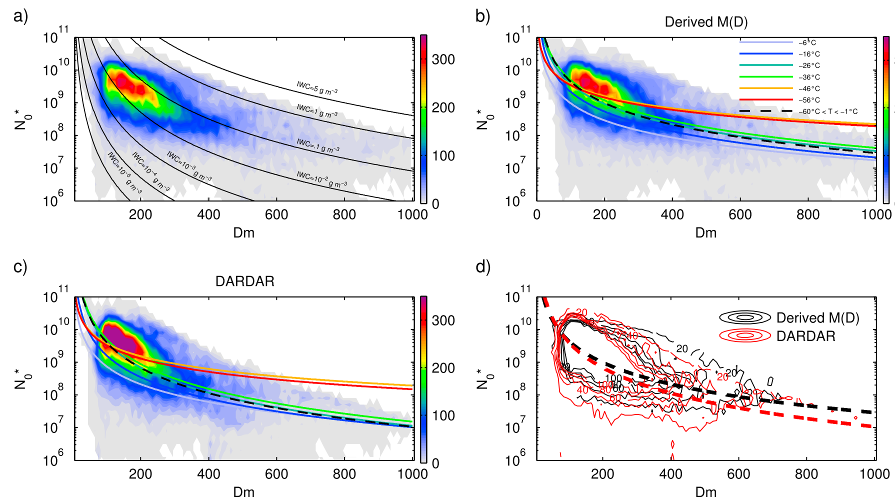

Figure 15. N_0^*-D_m relationships. (a) A PDF of N_0^* (m^{-4}) as a function of D_m (micron) computed using the measured PSD and retrieved $M(D)$. Black lines represent N_0^*-D_m relationships at constant IWC. (b) Identical to Figure 15a but including fits for each temperature range. (c) The same as Figure 15b assuming DARDAR $M(D)$. (d) Parameterizations obtained for the full range of temperature for the retrieved and DARDAR $M(D)$ are compared. Isocontours represent the number of data.

−10% +10% while the $N_0'(T)$ parameterization show a larger mean relative difference from −60% to 20%. If the first one produces the smallest differences for large IWC, it cannot be used for IWC < 0.001 g m^{-3}) as the absolute mean relative difference exceeds 300%.

The $N_0'(T)$ relationship is satisfactory as it produces an absolute mean difference smaller than 80% over the whole range. It is therefore obvious that the $N_0'(T)$ relationship is much more appropriate than the simple $N_0^*(T)$ parameterization; however, the extinction knowledge is required.

6.2. N_0^*-D_m Relationship

Figures 15a to 15c represent the PDF (probability distribution function) of N_0^* as a function of D_m. N_0^* and D_m are computed using the measured PSD and the retrieved $M(D)$ or DARDAR $M(D)$. As noted earlier there is an analytical relationship between D_m and N_0^*, and this relationship depends on IWC. These relationships are presented in Figure 15a, where each black line corresponds to a constant value of IWC. Contours show that most of the data are spanning 10^{-4} g m^{-3} and 1 g m^{-3}. It is also shown that the shape of the relationship is totally described by IWC. Unfortunately, in most cloud retrieval methods, IWC is unknown. Therefore, we are looking for a relationship between D_m and N_0^* which can be expressed as follows:

$$N_0^* = KD_m^L, \tag{23}$$

where K and L, reported in Table 6, are the best coefficients obtained by fitting the relationship between N_0^* and D_m in log space. They are computed for both $M(D)$, and the results are overplotted as a black or red dotted line. These coefficients can be computed for different ranges of temperature. Solid colored lines represent the parameterizations obtained for 10°C temperature intervals ranging from −6 to −56°C. These results illustrate that temperature affects the N_0^*-D_m relationship, with a jump near −36°C. Because small D_m and high N_0^* correspond to cold temperatures, the fit is calculated on a much smaller range of values and the representation of D_m above 400μm (cf. 7i) should not be taken into account.

Figure 15d presents the PDF as isocontours, with parameterizations derived for retrieved $M(D)$ and DARDAR $M(D)$. The change in the choice of the mass-size relationship does not affect the relationship between N_0^* and D_m.

Table 6. N_0^*-D_m Parameterization Coefficients

Mass-Size Relationship	K	L
Derived relationships [*Heymsfield et al.*, 2010]	1.07e14	−2.19
DARDAR	5.65e14	−2.57

The main effect is to contract or dilate the N_0^* and D_m ranges without significantly changing the parameterization. This is clearly an advantage and it is then possible to use the relationship between N_0^* and D_m as a priori information. Note

©2014. American Geophysical Union. All Rights Reserved.

that the idea is not to propose a very accurate parameterization and this is why we do not evaluate the error produced by using that parameterization. We show that it is possible to use this relationship to constrain a variational algorithm for instance by ensuring that the retrieved values belong to the envelope described by the contours [*Delanoë and Hogan*, 2008].

7. Summary and Discussion

The aim of the paper was to update the *Delanoë et al.* [2005] study on the normalized PSD approach. The main improvement resided in the use of a very large in situ data set including bulk measurements of the IWC. It also included direct measurements of the projected areas of the ice particles which allowed to compute a good proxy of visible extinction and could be combined with $M(D)$ to derive a realistic terminal fall velocity [*Heymsfield and Westbrook*, 2010]. We also proposed an optimized approach to derive the coefficients of the modified gamma representing the normalized PSD. A combination of two key measurement moments was presented for retrieving the coefficients. Once the coefficients are retrieved, we analyzed the impact of using the normalized approach for computing cloud and measurement variables. The impact of the temperature on the normalized PSD shape has been addressed in section 4.2. However, we have tried to parameterize the PSD shape as a function of temperature but the results were not conclusive and for this reason it was not presented in the study.

In section 5.4, the impact of $M(D)$ on the PSD shape retrieval was assessed. It was shown that the choice of the mass-size relationship did not change the conclusions regarding the benefit of the normalization approach. It was also obvious that the error in selecting the $M(D)$ was much larger than a wrong choice of the normalized modified gamma coefficients. This was not a surprise as it was clearly stated that most of errors come from $M(D)$ in cloud retrievals [*Heymsfield et al.*, 2010]. It could be envisioned to implement the normalized approach in the nonhydrostatic mesoscale atmospheric model of the French research community (Meso-NH) mesoscale model [*Lascaux et al.*, 2006]. A similar approach, using *Field et al.* [2007], has been introduced operationally on 17 January 2012 (PS28) in the UKMO global-scale model. The benefit would be the use of a single gamma shape representation for the different ice hydrometeor classes.

Appendix A: Impact of Small Particles on the PSD Shape

A1. Shattering Effect

As mentioned in section 3.2, the data used in this study are corrected from the shattering effect using particle interarrival times. The shattering effect can contaminate the number concentration of particles by artificially increasing the number of small particles which originates from the breakup of larger ice crystals on the probe's inlet. In this section, we examine the impact of the shattering correction on the results, by repeating the results presented in sections 4 and 5 but without the correction using particle interarrival times. We also introduce a shattering parameter, which varies between 0 and 1 and indicates the proportion of particles which have naturally occurring interarrival times as identified by the correction algorithm using Poisson counting statistics. Note that we consider a low-shattering environment to exist when this parameter is above 0.8. The impact of the shattering correction on the normalized PSD shape is presented in Figure A1. Figures A1a–A1c represent the normalized PSD when the particle concentration is not corrected from shattering, when it is corrected, and when only low-shattering environments are considered, respectively. The distribution of shattering parameter is shown in Figure A1f, and less than 23% of data are below the shattering parameter threshold. The contour plots (Figures A1a–A1c) show very similar patterns; however, the uncorrected normalized PSD distribution indicates a higher data concentration below $D_{eq}/D_m = 0.5$ than the corrected data. This is an expected result as the concentration of small particles is higher. When the data which are potentially prone to shattering contamination are removed, we observe even less data in the $D_{eq}/D_m < 0.5$ area. Figures A1d and A1e are idealized representations of the normalized PSD (modified gamma shape) for the corrected (black lines), uncorrected (red lines), and corrected with low-shattering environment (blue lines). The gamma modified (α, β) coefficients are derived using extinction and reflectivity (Figure A1d) or extinction only (Figure A1e). When (α, β) pair is derived using extinction and reflectivity, we can see that there are almost no changes in the results. However, we observe a difference in the results when we use only extinction to derive the (α, β) coefficients. The red and black curves are in very good agreement, but the shape corresponding to the "low-shattering" data is different when $D_{eq}/D_m > 2$. To evaluate the impact of using the corrected, uncorrected, or low-shattering data, we compute the relative

©2014. American Geophysical Union. All Rights Reserved.

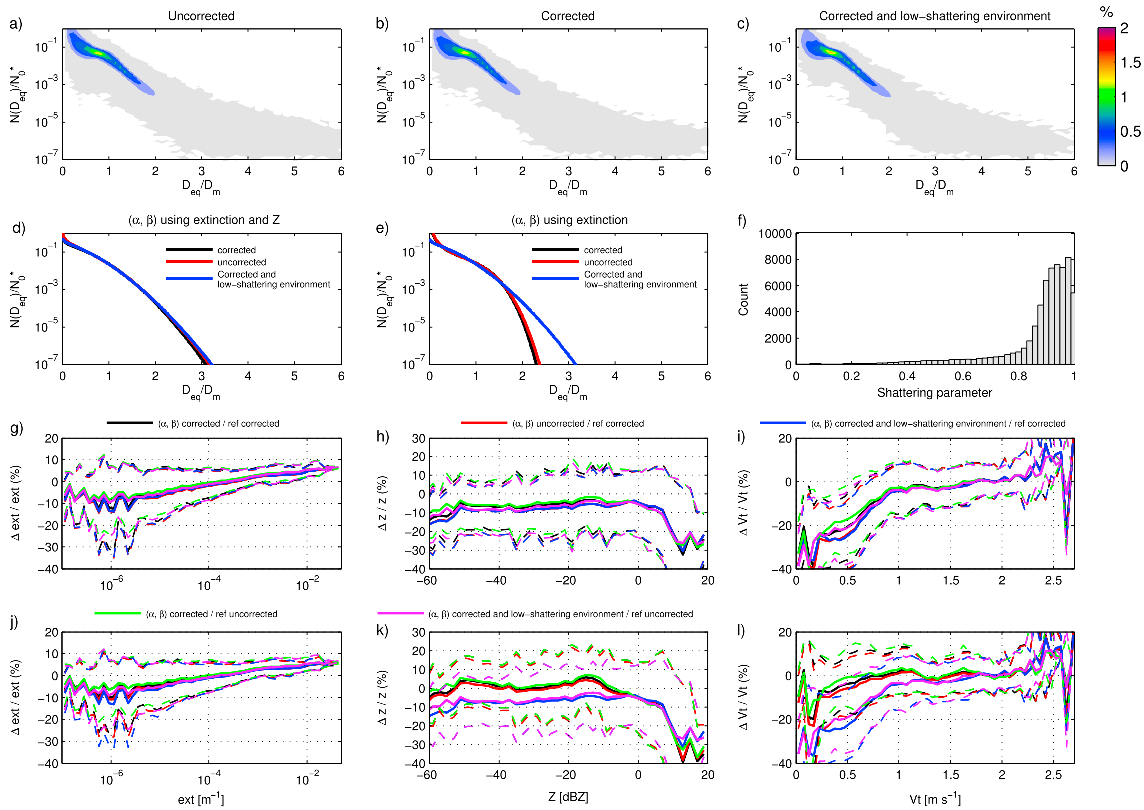

Figure A1. Impact of the shattering correction on the normalized PSD shape. The calculations involved PSD corrected and uncorrected from the shattering effects and also the corrected PSD when we have a low-shattering environment (see details in the text). (a–c) The normalized PSD. (d, e) Idealized representations of the normalized PSD. (f) The distribution of shattering parameter. Relative mean difference (in percent) between (g, j) extinction, (h, k) Z, and (i, l) V_t computed with the analytical gamma shape and the measured (corrected and uncorrected) PSD. Color codes are described in the text.

mean differences (in percent) between extinction for Figures A1g and A1j, Z for Figures A1h and A1k, and V_t for Figures A1i and A1l computed with the analytical gamma shape and the measured (corrected or uncorrected) PSD. Solid lines are the relative mean differences and the dashed lines are the ± 1 standard deviation. For these six panels, the color codes are the following:

1. Black lines - PSD coefficients are derived using the corrected PSD, and the reference (normalized extinction, normalized reflectivity, and terminal fall velocity) is the corrected PSD.
2. Red lines - PSD coefficients are derived using the uncorrected PSD, and the reference is the corrected PSD.
3. Blue lines - PSD coefficients are derived using the corrected and shattering coefficient greater than 0.8 PSD, and the reference is the corrected PSD.
4. Green lines - PSD coefficients are derived using the corrected PSD, and the reference is the uncorrected PSD.
5. Magenta lines - PSD coefficients are derived using the corrected and shattering coefficient greater than 0.8 PSD, and the reference is the uncorrected PSD.

We can consider that the impact of using the uncorrected, corrected, or shattering coefficient greater than 0.8 is not large when the coefficients are derived using extinction and reflectivity (Figures A1g–A1i). This is due to the fact that the reflectivity is not sensitive to small particles and counterbalances the impact on the extinction. We can use the coefficients derived using the corrected (with or without threshold on the shattering parameter) or uncorrected PSD to represent the normalized PSD if we are using radar and lidar measurements. However, the results are slightly different when only extinction is used to derived the normalized PSD coefficients. The change in the coefficients introduces biases in the retrieved Z (10% below -10 dBZ) and V_t (10% below 1.2 m s^{-1}). Note that the standard deviations are within the same range independently of the PSD used. Despite small changes in the PSD shape, we show that the presence of shattered particles does not change the main results of the study. Note that the data used in the main study are corrected from the shattering effects.

©2014. American Geophysical Union. All Rights Reserved.

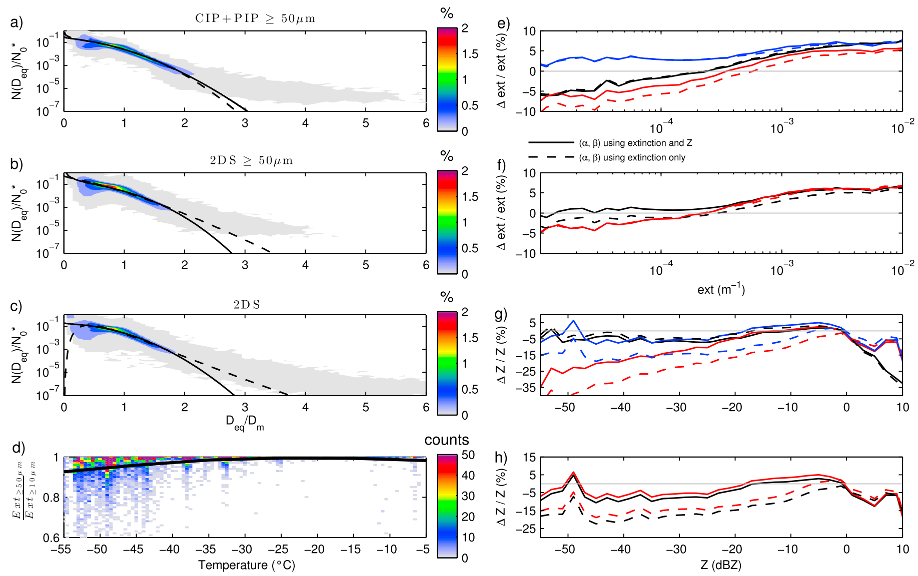

Figure A2. Impact of the small particle contribution on the normalized PSD shape. (a–c) The normalized PSD shapes for CIP+PIP data, 2D-S data when particles below 50 μm are removed and all 2D-S data, respectively. (d) The ratio of extinction derived using 2D-S data without small particles to extinction derived using all 2D-S data as a function of cloud temperature. (e–h) Relative differences (in percent) obtained with or without removing small particles. Details are in the text.

A2. Impact of Adding Particles Below 50 μm

The measurement of ice particles smaller than 50 μm is a challenging one from an aircraft [*Strapp et al.*, 2001], and only a few field programs available here had such measurements. For this reason we decided not to include particles below 50 μm in the main study. However, it is useful to verify that the main conclusions of the paper regarding the normalization are still valid. During the TC4 campaign, CIP, PIP, and 2D-S probes were available. The latter can measure down to 10 μm, and therefore, we can analyze the impact of using particles below this diameter. Figure A2 shows the result of using particles below 50 μm threshold. Note that the 2D-S are corrected from shattering effect (also using interarrival times). As a reference we show in Figure A2a the shape of the normalized PSD using CIP and PIP data above 50 μm. Figures A2b and A2c are the representations of the normalized PSD computed with 2D-S data with or without removing particle below 50 μm, respectively. While the general shape remains very similar (high concentration of data around $D_{eq}/D_m = 1$), we notice a few differences between the normalized PSD for $D_{eq}/D_m < 0.5$ and $D_{eq}/D_m > 2$. Solid and dashed lines represent the normalized gamma shape when (α, β) coefficients are derived using extinction and reflectivity and only extinction, respectively. The resulting shapes confirm the results of the contour plots.

Figure A2d is the ratio of extinction derived using 2D-S above 50 μm threshold to extinction derived using all 2D-S data as a function of cloud temperature. From this figure we can see that the change in extinction, which is due to particles below 50 μm removal, is mainly for cold temperature (i.e., below −40°C). This ratio reaches 0.92 at −55°C. This is an expected result as the proportion of small particles increases when clouds get colder. Figures A2e and A2f represent the relative mean differences (in percent) between the extinction calculated from the PSD ($D >$ 10 μm) and the extinction calculated using the normalized gamma shape. In Figure A2e, the black lines are the relative mean difference between extinction calculated using CIP+PIP measurements (excluding particles below 50μm) and extinction computed from the normalized gamma shape. The (α, β) coefficients are derived using extinction and reflectivity (solid line) and only extinction (dashed line) using CIP+PIP measurements. In Figure A2e, similarly, blue and red lines correspond to 2D-S data with and without small particles, respectively. Results are very similar for extinction values larger than $3 \times 10^{-4}\text{m}^{-1}$ where most of the data are concentrated (figure not shown). For lower extinctions, absolute values of relative difference are within the [−10% 10%] range, with overestimation of the extinction CIP+PIP measurements and 2D-S without small particles. Figure A2f represents the relative mean differences between extinction calculated from the 2D-S data with small particles and the extinction calculated using the normalized gamma shape and coefficients derived using the 2D-S data without small particles (black

©2014. American Geophysical Union. All Rights Reserved.

lines). Red lines are the results of relative mean difference obtained using (α, β) coefficients derived from extinction and reflectivity (solid line) and only extinction (dashed line) using small particles and when the reference extinction is computed without small particles. This shows that the presence of particles below 50 μm does not change the results for extinction. Figures A2g and A2h present the relative differences for radar reflectivity with the same color code. The presence of small particles has an impact of the retrieved coefficients, especially when only extinction is used to derive them. However, the impact of using particles below 50 μm does not contradict the main results presented in the main study.

Acknowledgments

Julien Delanoë's research is partly funded by CNES (Centre National d'Etudes Spatiales). For Andrew Heymsfield and Aaron Bansemer, support from the JPL CloudSat Project Office and CALIPSO Project Office, as well as from NASA GPM/PMM through contract NNX10AH67G are appreciated. We are also grateful to Carl Schmitt who processed Subvisible data. We also would like to thank the reviewers, whose thoughtful comments helped us improve the paper.

References

Brown, P. R. A., and P. N. Francis (1995), Improved measurements of the ice water content in cirrus using a total-water probe, *J. Atmos Oceanic. Technol.*, *12*, 410–414.

Delanoë, J., and R. J. Hogan (2008), A variational scheme for retrieving ice cloud properties from combined radar, lidar, and infrared radiometer, *J. Geophys. Res.*, *113*, D07204, doi:10.1029/2007JD009000.

Delanoë, J., and R. J. Hogan (2010), Combined CloudSat-CALIPSO-MODIS retrievals of the properties of ice clouds, *J. Geophys. Res.*, *115*, D00H29, doi:10.1029/2009JD012346.

Delanoë, J., A. Protat, J. Testud, D. Bouniol, A. J. Heymsfield, A. Bansemer, P. R. A. Brown, and R. M. Forbes (2005), Statistical properties of the normalized ice particle size distribution, *J. Geophys. Res.*, *110*, D10201, doi:10.1029/2004JD005405.

Delanoë, J., A. Protat, J. Testud, D. Bouniol, A. J. Heymsfield, A. Bansemer, and P. R. A. Brown (2007), The characterization of ice clouds properties from Doppler radar measurements, *J. Appl. Meteorol. Climatol.*, *46*, 1682–1698, doi:10.1175/JAM2543.1.

Field, P. R., R. J. Hogan, P. R. A. Brown, A. J. Illingworth, T. W. Chou-larton, and R. J. Cotton (2005), Parametrization of ice-particle size distributions for mid-latitude stratiform cloud, *Q. J. Roy. Meteorol. Soc.*, *131*, 1997–2017.

Field, P. R., A. J. Heymsfield, and A. Bansemer (2006), Shattering and particle interarrival times measured by optical array probes in ice clouds, *J. Atmos. Oceanic Technol.*, *23*, 1357–1371.

Field, P. R., A. J. Heymsfield, and A. Bansemer (2007), Snow size distribution parameterization for midlatitude and tropical ice clouds, *J. Atmos. Sci.*, *64*, 4346–4365.

Foot, J. S. (1988), Some observations of the optical properties of clouds. II. Cirrus, *Q. J. Roy. Meteorol. Soc.*, *114*, 145–164.

Heymsfield, A. J., and C. D. Westbrook (2010), Advances in the estimation of ice particle fall speeds using laboratory and field measurements, *J. Atmos. Sci.*, *67*, 2469–2482, doi:10.1175/2010JAS3379.1.

Heymsfield, A. J., C. Schmitt, A. Bansemer, and C. H. Twohy (2010), Improved representation of ice particle masses based on observations in natural clouds, *J. Atmos. Sci.*, *67*, 3303–3318, doi:10.1175/2010JAS3507.1.

Heymsfield, A. J., C. Schmitt, and A. Bansemer (2013), Ice cloud particle size distributions and pressure-dependent terminal velocities from in situ observations at temperatures from 0 to −86°C, *J. Atmos. Sci.*, *70*, 4123–4154, doi:10.1175/JAS-D-12-0124.1.

Hogan, R. J., L. Tian, P. R. A. Brown, C. D. Westbrook, A. J. Heymsfield, and J. D. Eastment (2012), Radar scattering from ice aggregates using the horizontally aligned oblate spheroid approximation, *J. Appl. Meteor. Climatol.*, *51*, 655–671.

Isaac, G., et al. (2005), First results from the Alliance Icing Research Study II, paper presented at 43rd AIAA Aerospace Sciences Meeting and Exhibit, American Institute of Aeronautics and Astronautics, Reno, Nevada.

Lascaux, F., E. Richard, and J.-P. Pinty (2006), Numerical simulations of three different MAP IOPS and the associated microphysical processes, *Q. J. R. Meteorol. Soc.*, *132*, 1907–1926.

Lawson, R. P., and B. A. Baker (2006), Improvement in determination of ice water content from two-dimensional particle imagery. Part II: Applications to collected data, *J. Appl. Meteorol. Climatol.*, *45*, 1291–1303, doi:10.1175/JAM2399.1.

Lee, G. W., I. Zawadzki, W. Szyrmer, D. Sempere-Torres, and R. Uijlenhoet (2004), A general approach to double-moment normalization of drop size distributions, *J. Appl. Meteor.*, *43*, 264–281.

Mitchell, D. (1996), Use of mass- and area-dimensional power laws for determining precipitation particle terminal velocity, *J. Atmos. Sci.*, *53*, 1710–1723.

Schmitt, C. G., and A. J. Heymsfield (2009), The size distribution and mass-weighted terminal velocity of low-latitude tropopause cirrus crystal populations, *J. Atmos. Sci.*, *66*, 2013–2028.

Sekhon, R. S., and R. C. Srivastava (1971), Doppler radar observations of drop-size distributions in a thunderstorm, *J. Atmos. Sci.*, *28*, 983–994.

Strapp, J. W., F. Albers, A. Reuter, A. V. Korolev, U. Maixner, E. Rashke, and Z. Vukovic (2001), Laboratory measurements of the response of a PMS OAP-2DC, *J. Atmos. Oceanic Technol.*, *18*, 1150–1170, doi:10.1175/1520-0426(2001)018<1150:LMOTRO>2.0.CO;2.

Szyrmer, W., A. Tatarevic, and P. Kollias (2012), Ice clouds microphysical retrieval using 94-GHz Doppler radar observations. Part I: Basic relations within the retrieval framework, *J. Geophys. Res.*, *117*, D14203, doi:10.1029/2011JD016675.

Testud, J., S. Oury, R. A. Black, P. Amayec, and X. K. Dou (2001), The concept of "normalized" distribution to describe raindrop spectra: A tool for cloud physics and cloud remote sensing, *J. Appl. Meteor.*, *40*, 1118–1140.

Toon, O. B., et al. (2010), Planning, implementation, and first results of the Tropical Composition, Cloud and Climate Coupling Experiment (TC4), *J. Geophys. Res.*, *115*, D00J04, doi:10.1029/2009JD013073.

Twohy, C. H., A. J. Schanot, and W. A. Cooper (1997), Measurement of condensed water content in liquid and ice clouds using an airborne counterflow virtual impactor, *J. Atmos. Oceanic Technol.*, *14*, 197–202.

Verlinde, J., et al. (2007), The mixed-phase arctic cloud experiment, *Bull. Amer. Meteorol. Soc.*, *88*, 205–221, doi:10.1175/BAMS-88-2-205.

©2014. American Geophysical Union. All Rights Reserved.